Internal Report
DESY F31-85-01
April 1985

INCLUSIVE PHOTON SPECTRUM OF Υ(2S)-DECAYS

by

R. Nernst

INCLUSIVE PHOTON SPECTRUM OF $\Upsilon(2S)$-DECAYS

Dissertation
zur Erlangung des Doktorgrades
des Fachbereichs Physik
der Universität Hamburg

vorgelegt von
Ralf Nernst
aus Hamburg

Hamburg
1985

Gutachter der Dissertation : Prof. Dr. U. Strohbusch
Prof. Dr. J.K. Bienlein

Gutachter der Disputation : Prof. Dr. E. Hilger
Prof. Dr. U. Strohbusch

Datum der Disputation : 22.März 1985

Sprecher des
Fachbereichs Physik und
Vorsitzender des
Promotionsausschusses : Prof. Dr. J. Appel

CONTENTS

1.0 ABSTRACT

The Crystal Ball detector has been used at the e^+e^--storage ring DORIS II to search for radiative transitions from the $\Upsilon(2S)$. The data were taken between August 1982 until February 1984. Using the inclusive photon spectrum from the hadronic decays of the $\Upsilon(2S)$ three well resolved low energy lines are observed and their energies are measured to be :

$110.6 \pm 0.8 \pm 2.2$ MeV

$130.9 \pm 0.8 \pm 2.4$ MeV

$163.3 \pm 1.5 \pm 2.7$ MeV

The corresponding branching ratios are :

110 MeV : $5.9 \pm 0.7 \pm 1.0$ %

131 MeV : $6.5 \pm 0.6 \pm 1.2$ %

163 MeV : $3.7 \pm 0.7 \pm 0.9$ %

A fourth line around 430 MeV is interpreted as the sum of two Doppler broadened lines. The sum of the product branching ratios for the transitions

$\Upsilon(2S) \to \gamma 1^3P_{2,1} \to \gamma\gamma\Upsilon(1S)$ is found to be :

$3.4 \pm 0.7 \pm 0.5$ %

By clearly resolving all 3 low energy lines in the inclusive photon spectrum from hadronic decays of the $\Upsilon(2S)$ a complete measurement of the fine splitting of the $1^3P_{2,1,0}$ states of the $b\bar{b}$ system has been made.

No other photon lines are observed with statistical significances of more than 2.3 standard deviations in the energy range 50 - 100 MeV giving an upper limit for branching ratios of 2.3 % (90 % c.l.). In the range 450 - 850 MeV an upper limit of 0.7 % (90 % c.l.) is obtained.

2.0 INTRODUCTION

The discovery of the $\Upsilon(1S)$ /HERB77/ and $\Upsilon(2S)$ resonance /INNE77/ in the mass spectrum of dimuons produced in proton-nucleon collisions at Fermilab in Batavia,Illinois(U.S.A.) inspired an effort to produce these resonances also in electron positron annihilation. The experiments PLUTO and DASP at the e^+e^--storage ring DORIS at DESY in Hamburg,Germany confirmed the existence of the $\Upsilon(1S)$ resonance /BERG78/,/DARD78/. Later the DESY-Heidelberg detector (which replaced PLUTO) and DASP II also observed and measured some of the properties of the $\Upsilon(2S)$/BIEN78/,/DARD78a/.

In 1979 the Cornell Electron Storage Ring (CESR) at Ithaca,New York (U.S.A.) came into operation and the 2 experiments there,CUSB and CLEO,discovered another state,now called $\Upsilon(3S)$ /BÖHR80/,/ANDR80/.

The above mentioned resonances are interpreted as bound $^3S_1$ states of the beauty quark (b) and the corresponding antiquark ($\bar{b}$). Later the $\Upsilon(4S)$ was found /ANDR80a/,FINO80/ which lies just above the threshold for the decay of the resonance into a $B\bar{B}$ meson pair /BEBE81/,/CHAD81/.

After the discovery of these states one started to look for transitions between the $^3S_1$ states as well as transitions to other levels (e.g.^3P_J states) similar to the transitions seen in the charmonium system /PART84/. Some of the possible transitions can be seen from an expected level scheme of the $b\bar{b}$ system in Figure 1 on page 3.

The dipion transition $\Upsilon(2S) \to \pi^+\pi^-\Upsilon(1S)$ was first observed by the LENA-collaboration /NICZ81/ using the DESY-Heidelberg detector. $\pi^+\pi^-$-transitions from the $\Upsilon(3S)$ to the $\Upsilon(2S)$ and $\Upsilon(1S)$ were found by CUSB /MAGE81/ and CLEO /MUEL81/,/GREE82/ at CESR.

The first direct evidence for 2^3P_J states was reported by the CUSB-group both in their inclusive photon spectrum/HANO82/ and the exclusive channel /EIGE82/ :

$$\Upsilon(3S) \to \gamma 2^3P_J \to \gamma\gamma\Upsilon(1S) \text{ or } \Upsilon(2S) \to \gamma\gamma l^+l^- (l = e \text{ or } \mu)$$

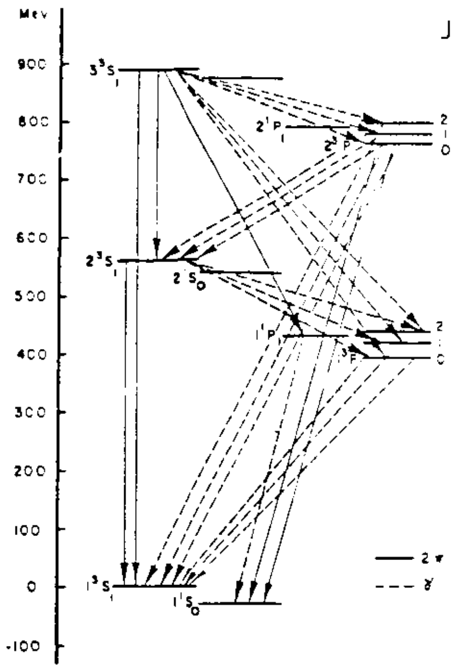

Figure 1. Expected level scheme and transitions between bound $b\bar{b}$ states

In April 1982 the Crystal Ball experiment was moved from the SPEAR storage ring at Stanford,California(U S A) to the upgraded DORIS II at DESY.

The Crystal Ball detector is designed to provide excellent energy and angular resolution for photons with high detection efficiency over nearly the entire solid angle Thus it was hoped that the detector could make a similar contribution to $b\bar{b}$ spectroscopy as it had to $c\bar{c}$ spectroscopy /GAIS82/,/OREG82/,/RPAR80/. Here the detector had played an important role in measuring the energies and radiative transition rates from the Ψ' to the $1^3P_{2,1,0}$ and the 1^1S_0,2^1S_0 states.

In 1983 all 4 experiments at CESR and DORIS II reported results on the radiative transitions from the $\Upsilon(2S)$ to the 1^3P_J states in

inclusive photon spectra /KLOP83/,/TUTS83/,/SCHW83/,/GALI83/ and the exclusive channel /PAUS83/ :

$\Upsilon(2S) \to \gamma\gamma l^+l^-$, leptons from $\Upsilon(1S)$

While there was reasonable agreement on the energies of the 2 lines around 108 and 128 MeV no experiment was able to make a statistically significant measurement of the expected third line (CUSB 2.5 standard deviations,CLEO : < 2,ARGUS 2.2 ,Crystal Ball: no signal) The line corresponding to the decay of the 1^3P_0 state is expected to have a small radiative transition rate to the $\Upsilon(1S)$ /NOVI78/ and is therefore difficult to see in the exclusive channel $\Upsilon(2S)\to\gamma\gamma l^+l^-$,but it should be possible to observe it in the inclusive photon spectrum.

A statistically more significant measurement (3.7 standard deviations) for a third line was given by the Crystal Ball collaboration in March 1984 /IRIO84/ based on preliminary results using a limited data sample.

So far no evidence has been found for other transitions from the $\Upsilon(2S)$ with significant branching fractions,e.g. to the 1^1S_0 or 2^1S_0 states

In the following chapters Crystal Ball results on the inclusive photon spectrum from hadronic decays of the $\Upsilon(2S)$ are presented for the full data sample The energies and branching ratios for the photon lines corresponding to radiative transitions from the $\Upsilon(2S)$ to the 1^3P_J states and from the 1^3P_J states to the $\Upsilon(1S)$ are given The results are compared with those of other experiments and theoretical predictions.

3.0 ELECTRON-POSITRON ANNIHILATION PROCESSES

In this chapter the fundamental e^+e^--annihilation processes and definitions which will be used later on are introduced.

The most common processes in e^+e^--annihilation are :

1 the purely electromagnetic pair production processes which can be described by QED (Quantum Electrodynamics) :

$$e^+ e^- \;{-}{-}{-}{-}{>}\; e^+ e^- (\gamma)$$
$$e^+ e^- \;{-}{-}{-}{-}{>}\; \mu^+ \mu^-(\gamma)$$
$$e^+ e^- \;{-}{-}{-}{-}{>}\; \tau^+ \tau^-(\gamma)$$
$$e^+ e^- \;{-}{-}{-}{-}{>}\; \gamma\, \gamma\, (\gamma)$$

2. the resonant and non-resonant hadron production described by QCD (Quantum Chromodynamics).

$$e^+ e^- \;{-}{-}{-}{-}{>}\; \text{hadrons}$$

3.1 μ- and τ-Pair Production

The simplest of all QED-reactions is the production of μ- and τ-pairs and can be calculated using the following Feynman diagram :

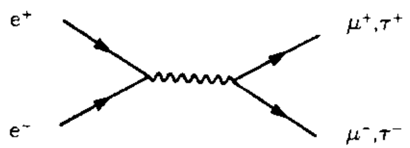

The original electron und positron annihilate and form a virtual photon which then materializes into a pair of leptons ($\mu^\pm,\tau^\pm$).

The production cross section σ is given by :

$$\sigma(e^+e^- \to \mu\mu,\tau\tau) = \frac{4\pi\alpha^2}{3\ S}\ \beta\ \frac{(3 - \beta^2)}{2} \qquad (1)$$

where β is the velocity of the particle divided by the speed of light at a c.m.s. energy $\sqrt{S}$ and α is the fine structure constant. At high c.m.s. energies ($\approx$ 10 GeV) the mass of the muon can be neglected,hence $\beta \to 1$ and the formula simplifies to :

$$\sigma(e^+e^- \to \mu^+\mu^-) = \frac{4\pi\alpha^2}{3\ S} \approx \frac{87.6\ \text{nb}}{S} \qquad (S \text{ in GeV}) \ (2)$$

3.2 BHABHA SCATTERING($e^+e^- \to e^+e^-$)

In addition to the annihilation Feynman diagram there is an additional diagram which contributes to the cross section for this process :

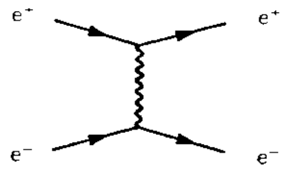

The differential cross section $d\sigma/d\Omega$ rises steeply at small angles to the beam. This process is used to measure the Small-Angle-Bhabha luminosity (see "Luminosity Monitor"). Bhabhas are also used later on to calibrate the crystals (see "Energy Calibration").

3.2.1 Luminosity

An important parameter to determine the performance of a storage ring is the luminosity. If the numbers of particles per bunch are n_1 and n_2,the rotation frequency f,the geometric cross section of the beams q and the number of bunches per beam b,then the luminosity l is given by :

$$l = \frac{n_1\ n_2\ f\ b}{q} \qquad (3)$$

As the determination of the parameters is difficult (especially the beam cross section), one uses a process with a high rate where the cross section can be reliably calculated and measured. Such a process are Bhabhas scattered under small angles to the beam (see "Luminosity Monitor"). From a measured integrated luminosity $L = \int l dt$ the cross section σ for a reaction is given by :

$$\sigma = \frac{N}{L} \tag{4}$$

where N is the number of events observed,corrected for the measurement efficiency.

3.3 TWO PHOTON ANNIHILATION

Another annihilation process which can be described by QED is the pair production of two real photons :

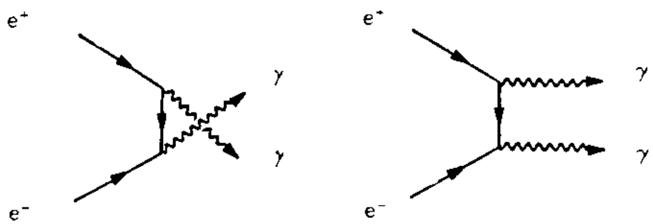

There are 2 Feynman diagrams because the 2 final state particles are identical. As electrons and photons have the same behaviour in the Crystal Ball (if one ignores the charge information), photons from this reaction are also used for energy calibration.

3.4 HADRON PRODUCTION

According to the quark model /GELL64/ hadrons are composed of quarks. Mesons can be constructed from a quark-antiquark combination ($q\bar{q}$) while baryons consist of 3 quarks(qqq). For every one of the 6 quarks(flavours) there is also an antiquark($\bar{q}$). Every quark has spin 1/2 and a charge of -1/3 for the flavours d,s,b and 2/3 of the elementary charge for the u,c and t quarks. For every flavour there are 3 different colours.

3.4.1 Non-resonant Hadron Production

The description of non-resonant production of hadrons is based on 2 assumptions:

1. The virtual photon creates a quark-antiquark pair through a purely electromagnetic interaction. This is simply the reaction desribed for muons mentioned above with an additional factor, the square of the quark charge Q,where Q is given in units of the electron charge.

2. All $q\bar{q}$ pairs materialize as hadrons,free quarks cannot exist.

Two 2 jets of hadrons should be seen, meaning that the resulting hadrons from the fragmentation are boosted in the direction of the original quark with a limited transverse momentum to the quark direction.

The cross section is given by :

$$\sigma(e^+e^- \to q\bar{q}) = \frac{4\pi\alpha^2}{3S} \cdot \beta \frac{(3-\beta^2)}{2} \sum 3Q_i^2 \tag{5}$$

where one sums over all possible flavours i at a certain energy $\sqrt{S}$. The factor 3 accounts for the three possible 'colours' for each flavour. The second assumption that all $q\bar{q}$ combinations decay into hadrons means that the cross section for hadron production is the same as for $q\bar{q}$ production.

$$\sigma(e^+e^- \to q\bar{q}) = \sigma(e^+e^- \to \text{hadrons}) \tag{6}$$

The ratio of the hadron production cross section to the asymptotic μ-pair cross section is called R and the advantage is that the energy dependence cancels out :

$$R = \frac{\sigma(e^+e^- \rightarrow \text{hadrons})}{\sigma(e^+e^- \rightarrow \mu\mu)} \tag{7}$$

For c.m.s. energies far above a flavour threshold (Energy >> 2 times the quark mass) this becomes :

$$R = \sum 3\ Q_i^2 \tag{8}$$

3.5 RESONANCE PRODUCTION

At certain c.m.s. energies a quark and antiquark form a bound state (resonance). The system is held together by the colour force mediated by vector gluons in a fashion analogous to the electromagnetic force for atoms or positronium,which is a system of an electron and a positron (bound by a virtual photon). $q\bar{q}$ states are refered to as quarkonia (charmonium for $c\bar{c}$ and bottomonium for $b\bar{b}$). In contrast to photons gluons carry a so called charge,the colour charge.

The experimentally found OZI(Okubo,Zweig,Iizuka)-rule/OKUB63/ says that decays where the original quark and antiquark appear in the final state are broad while states where the q and $\bar{q}$ have to annihilate are narrow (e.g. the $\Upsilon(1S)$).

OZI-suppressed decays should occur via intermediate gluons leading to small total widths. The minimum number of gluons (which will decay into hadrons) allowed by conservation laws for states which have the same quantum numbers as a photon are three :

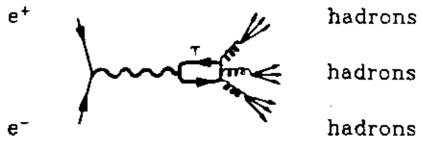

One intermediate gluon is not allowed as the produced hadrons carry no colour charge. Two are ruled out because a spin 1 state cannot decay into 2 massless gluons of spin 1 (this would violate parity conservation rules). One expects three jets from the fragmentation of the 3 gluons which should look somewhat different from the 2-jet structure for the non-resonant hadron production.

OZI-allowed decays occur above the flavour threshold where the original q and $\bar{q}$ appear in the final state ,e.g.$\Upsilon(4S) \rightarrow B\bar{B}$ where B is a meson carrying the flavour beauty /BEBE81/,/CHAD81/ :

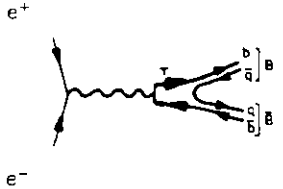

3.5.1 Quantum numbers of the $b\bar{b}$ levels

The quantum numbers of the $b\bar{b}$ levels are a consequence of the spin 1/2 nature of the quark and antiquark. They are denoted by J,the total angular momentum of the meson,P the parity $P=(-1)^{L+1}$ and C the charge parity $C=(-1)^{L+S}$ for spin S and orbital angular momentum L. In spectroscopic notation the states are labelled by $n^{2S+1}L_J$ with the radial quantum number n.

Orbital angular momentum L=0 leads to vector(triplet) states n^3S_1 where the spins of the quarks are parallel (e.g. the J/Ψ,$\Upsilon(1S)$) and to pseudoscalar(singlet) states n^1S_0(e.g. the so called η_c in the charmonium system) where the spins are anti parallel. The resonance having the smallest mass (e.g.$\Upsilon(1S)$) is considered to be the ground state and the $\Upsilon(2S)$,$\Upsilon(3S)$... are the radially excited states.

Some of the expected properties of the more easily produced states are discussed below.

3.5.2 $^3S_1$ States

The $^3S_1$ states have an orbital angular momentum of L=0 and odd parity and charge conjugation and can therefore be produced directly in e^+e^--annihilation as they have the same quantum numbers as a photon

3.5.3 $^3P_{2,1,0}$ States

The ^3P_J states have an orbital angular momentum of L=1, even parity and charge conjugation. This means that they cannot be produced directly in e^+e^--annihilation but can be reached by radiative transitions from higher lying $^3S_1$ states. The ^3P_J states are thought to decay hadronically via gluon annihilation or by a radiative decay into lower lying $^3S_1$ states. In lowest order QCD the 0^{++} and 2^{++} can decay via 2 gluon emission, whereas the 1^{++} must emit 3 gluons or a gluon-quark-antiquark combination /KRAS79/.

The decays $\Upsilon(2S)\to\gamma^3P_J$ proceed in lowest order via electric dipole(E1)-transitions. For an E1-transition the angular distribution $W(\Theta)$ of the photon with respect to the beam axis is of the form :

$$2^3S_1 \to \gamma 1^3P_0 : \quad W(\Theta) \propto 1 + \cos^2\Theta$$

$$2^3S_1 \to \gamma 1^3P_1 : \quad W(\Theta) \propto 1 - 1/3 \cos^2\Theta$$

$$2^3S_1 \to \gamma 1^3P_2 : \quad W(\Theta) \propto 1 + 1/13 \cos^2\Theta$$

For the the J=1,2 states higher multipole terms could also contribute but are expected to be small /BROW76/.

The radiative transitions between the $^3S_1$ and ^3P_J states can be seen in decays of the excited $^3S_1$ states as discrete lines in the

photon spectra from either hadronic events or exclusive decay channels. In principle it should be possible to distinguish between the different spins by means of the angular distribution of the photons. Unfortunately in inclusive searches the lines reside on a large background. Therefore one can expect spin assignments only from exclusive searches.

3.5.4 $^1S_0$ States

The $^1S_0$ states have $J^{PC}=0^{-+}$ and can be reached from the $^3S_1$ states via radiative M1(spin flip)-transitions. They are supposed to lie below their corresponding vector states but the expected branching ratios are below the sensitivity of this experiment ($\approx 10^{-4}$) /FRID84/.

3.5.5 $^1P_1$ States

These states have $J^{PC}=1^{+-}$. Because of the odd C-parity they cannot be reached from $^3S_1$ states by photon transitions. As yet no $^1P_1$ state has been discovered either in the charmonium or in the bottomonium system. Their mass is expected to be about the same as the centre of gravity for the corresponding ^3P_J states. A possible transition to reach them is via 2 pions but if the mass difference between $^3S_1$ and the $^1P_1$ state is less than twice the π-mass it cannot be reached.

3.6 POTENTIAL MODELS

In order to calculate the position of levels the splittings and E1-transition rates a potential for the colour force has to be postulated. The potential should be flavour independent to describe both the $c\bar{c}$ and $b\bar{b}$ family.

In most calculations the bound $q\bar{q}$ system is described by a non-relativistic Schrödinger equation assuming that the quarks are sufficiently heavy. The forces acting between the quarks are approximated by a steeply rising attractive potential at short distances. Here the force can be represented by single-gluon exchange. A linear term is added to ensure quark confinement at long ranges as there should be no free quarks :

$$V_{NR}(r) = -\frac{4\alpha_s}{3\,r} + kr \qquad (9)$$

where α_s is the strong coupling constant and r is the mean radius of the system. k is a constant which has to be determined.

The potentials are of the form :

$$V(r) = V_{NR}(r) + V_1 + V_2 + V_3$$

V_1,V_2 and V_3 are relativistic corrections to the non relativistic potential V_{NR} where V_1(spin-orbit coupling), V_2(spin-spin coupling) and V_3(tensor force) are responsible for the fine splitting and hyperfine splitting of triplet and singlet states.

The experimental results obtained in the charmonium system can be used to fix the parameters of the potential if flavour independence is assumed. Various forms of the potential have been proposed (/BHAN78/,/EICH80/,/MART80/, /QUIG77/ and /RICH79/). Which potential describes the data best can be determined by experiments. Unfortunately the $b\bar{b}$ system is not heavy enough to probe the very short distance behaviour of the potential (< 0.1 fm) to discriminate among the different approaches. In the range of the Υ(1S),Υ(2S) all potentials show a similar behaviour as can be seen from Figure 2 where the values of the different potentials are plotted as a function of their mean radius r.

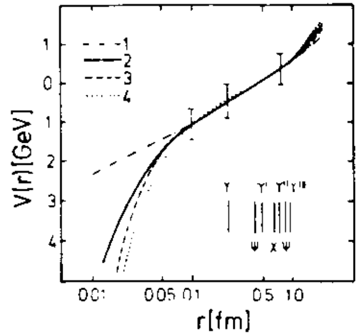

Figure 2. Values of the potentials quoted in the text: 1:/MART80/,2:/BUCH80/,3:/BHAN78/ ,4:/EICH80/.This figure is taken from /BUCH81/

3.6.1 Predictions for the Masses of the $^3P_{2,1,0}$ States

In general the masses of the $^3P_{2,1,0}$ states are given by the expectation values for the spin-orbit coupling (L·S) and the tensor force (S_{12}) :

$$M(^3P_J) = M_{cog} + a \langle L{\cdot}S\rangle + b \langle S_{12}\rangle \qquad (10)$$

with the centre of gravity M_{cog} given by :

$$M_{cog} = \frac{\sum M_J(2J+1)}{\sum 2J+1} \qquad (11)$$

where M_J are the masses for the different total angular momenta J of the states.

Using the <L·S> and $<S_{12}>$ as given in /MCCL83/ the masses of the $^3P_{2,1,0}$ become :

$$
\begin{aligned}
M(^3P_2) &= M_{cog} + a - 2/5\ b \qquad (12)\\
M(^3P_1) &= M_{cog} - a + 2\ b\\
M(^3P_0) &= M_{cog} - 2a - 4\ b
\end{aligned}
$$

By knowing the fine splitting of the ^3P_J states one can determine how the tensor force influences the fine structure splitting or if it is needed at all to describe it (b=0).

The ratio of the level splittings $^3P_2$-$^3P_1$ and $^3P_1$- $^3P_0$ should be 2 if there is no tensor force assumed.

4.0 EXPERIMENTAL LAYOUT

4.1 DORIS II

DORIS was originally designed as a double storage ring with one ring on top of the other and 2 interaction regions where electrons and positrons collided. In 1978 DORIS was operated as a single ring machine using only the upper ring and increasing the the maximum centre of mass energy from 7 to 10.2 GeV to be able to measure in the $\Upsilon(1S)$ and $\Upsilon(2S)$ energy range /DORI79/.

In order to allow measuring higher $b\bar{b}$ resonances with higher luminosity DORIS II was planned, constructed and came into operation in April 1982. This included the removal of one of the rings,modifications of the bending magnets and the installation of mini-beta quadrupole magnets (strong focussing magnets) which had to be integrated into the detectors very close to the interaction regions. The maximum energy is now 11.2 GeV. Averaged over longer periods of time an integrated luminosity of 600 nb^{-1} per day has been achieved with peaks around 1000 nb^{-1}/day at 10 GeV with currents around 30 mA /NESE83/. The 2 interaction regions are occupied by the ARGUS (south) and the CRYSTAL BALL detector (north side) as one can see from Figure 3 where DORIS II is shown with its injection systems and experiments.

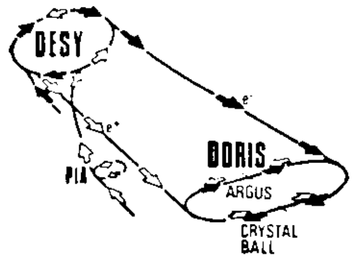

Figure 3. DORIS II with its injection system (DESY and PIA) and its experiments Crystal Ball and ARGUS

4.2 CRYSTAL BALL

The CRYSTAL BALL detector is best suited to resolve photon lines in energy ranges from a few MeV up to several GeV with good energy resolution of $\sigma(E)/E = 2.7\ \% / \sqrt[4]{E}$ (E in GeV). As a non-magnetic detector it cannot measure the momenta of charged particles except for electrons which deposit almost all of their energy in the ball at DORIS II energies. It should be noted that in the following electrons always refers to electrons and positrons because they cannot be distinguished by their behaviour in the energy detector. It is possible to check if a particle was charged but not to determine the sign of the charge.

The detector was operated at the e^+e^--storage ring SPEAR at SLAC (Stanford Linear Accelerator Centre) at Stanford,California (U.S.A.) from fall 1978 until the end of 1981 to look for photon transitions between bound $c\bar{c}$ states. Then it was decided to move the experiment to DESY (Deutsches Elektronen Synchrotron) in Hamburg,Germany to do a similar spectroscopy for the $b\bar{b}$ resonances. Several parts of the apparatus had to be rearranged and modified and new ones were put in. The layout of the most important components can be seen in Figure 4 and they will be described in the following sections.

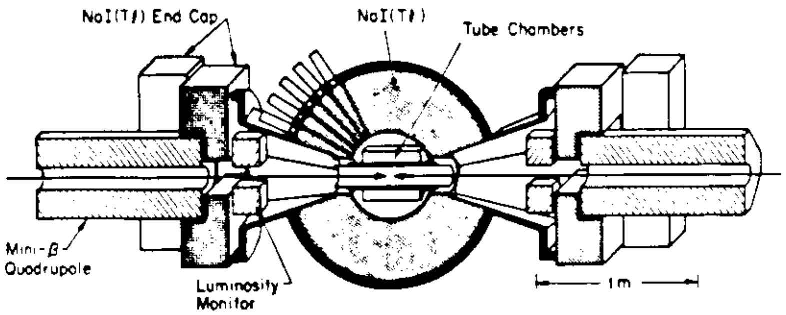

Figure 4. The main components of the Crystal Ball at DORIS II

4.2.1 Energy Detector

The NaI(Tl) is the central component of the Crystal Ball detector. Its purpose is to measure the energy and directions of photons resulting from e^+e^--annihilations occurring at the centre of the detector. The segmented spherical shell consists of 672 optically isolated thallium doped sodium iodide crystals. It has an inner radius of 25 cm and an outer one of 66 cm.

This corresponds to 15.7 radiation lengths for showering particles (photons,electrons) which typically deposit their energy in several crystals with a very symmetric shower pattern.

For strongly interacting particles ($\pi^{\pm}$,$K^{\pm}$,p) this corresponds to approximately one nuclear absorption length of NaI(Tl). This results in about 2/3 of the final state hadrons interacting with other nuclei in the detector. They initiate a hadronic shower much of which leaks out the rear of the crystals so that an accurate energy measurement cannot be made. The distribution of energy deposited by charged hadrons in the NaI(Tl) peaks around 210 MeV due to non-interacting minimum ionizing charged particles and has a long tail towards higher energies due to nuclear interactions.

A disadvantage in using NaI is that it is hygroscopic and cannot be exposed to air as this would irreparably damage its optical properties. Therefore the crystals are hermetically sealed in two hemispherical containers to protect them from water vapour in the atmosphere. In addition all the components of the detector displayed in Figure 4 are inside a 'dryhouse' where the air is kept at a constant and very low humidity.

4.2.2 Geometry and jargon

The basic principle for the construction of the Crystal Ball is an icosahedron. Each of the 20 faces (called 'major triangles') is subdivided into 4 smaller 'minor triangles' which in turn are made up by 9 individual crystals (or modules) as can be seen in Figure 5. Their vertices are projected back onto the sphere to make up the final geometry. This would add up to 720 crystals but 48 had to be removed in order to accommodate the beam pipe which leaves 336 crystals for each of the 2 hemispheres.

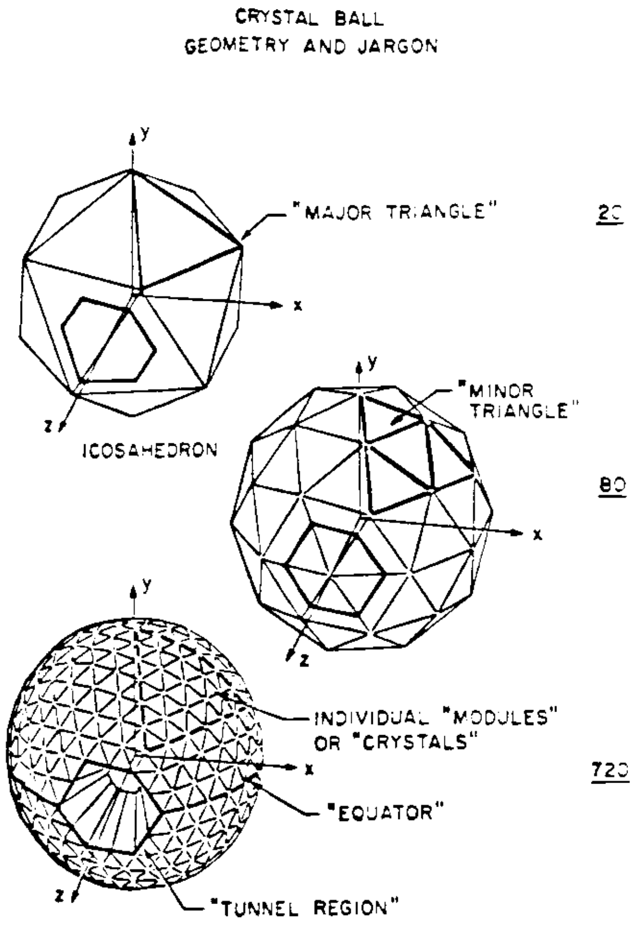

Figure 5. CB geometry and nomenclature (from /OREG80/)

The ball covers 93 % of the full solid angle.

The spherical coordinate system of the detector is taken so that the positron direction defines the positive z-axis. The x-axis points to the centre of the ring. The polar angle is denoted by Θ and the azimuthal angle by Φ.

'Tunnel modules' refers to the first layer of crystals surrounding the beam pipe, 'equator crystals' are those adjacent to the x-z plane.

Further details of the construction can be found in /CHAN78/ and /OREG80/.

4.2.3 Endcaps

In order to enlarge the solid angle for particle detection in the tunnel regions additional NaI crystals were used. The endcap configuration used at SPEAR had to be rearranged for DORIS II to accommodate the minibeta quadrupole magnets. 20 crystals in each tunnel region improve the solid angle from 93 to 98 % of 4π. For showering particles coming from the interaction region they have a depth of 3-9 radiation lengths of NaI. These crystals are not used for the energy measurement of photons in this analysis because of their short depth in radiation lengths.

4.2.4 Tube chambers

Inside the cavity of the ball is the inner detector to detect charged particles using 3 double layers of drift tubes with charge division readout. The first and second layer each consisted of 2*80 tubes while the outer one has 2*160.

In spring 1983 the inner 2 double layers were replaced by a new set of 2*64 tubes for the inner and 2*76 for the middle layer. The 3 double layers cover the total angular range in Φ and 98,96 and 75 % of the full solid angle (for both chamber configurations). The angular resolution is 1-2 ° in Φ and in z it amounts to to 1.2 % of the active lengths which are 68.6,53.3 and 35.6 cm respectively /HORI84/.

The detection efficiency for charged particles is very dependent on the hardware performance of the tubes (e.g. broken wires and amplifiers). For the third chamber by itself the detection efficiency varied between 85 % for the beginning of the datataking and 50 % near the end.

The probability that a photon coming from the interaction region at an angle perpendicular to the beamline is misidentified as a charged particle is given by the probability that a photon converts to an electron-positron pair in the beam pipe (1.7 %) or the first two layers of tubes (1.3 (2.5) % for each of the old (new) chambers). In addition they have to be detected by the outer chamber. In the following the total probability for detection of the conversion will be called conversion probability. The number used in this analysis (see "Photon Detection Efficiency") is obtained by integrating the conversion probability over the solid angle which is covered by the third chamber taking into account the luminosity weighted conversion probability for the two different chamber configurations and the measured chamber efficiencies. The calculated conversion probability is 4.6 ± 0.4 %.

4.2.5 Luminosity Monitor

Another part of the detector which had to be rearranged for DORIS II is the luminosity monitor which monitors the performance of the storage ring. The integrated Small-angle-Bhabha luminosity (SAB) is calculated by dividing the number of found Bhabhas by the well known QED cross section for Bhabha scattering integrated over the geometric acceptance of the counter (using Eq.(4)).

The monitor is mounted above and below the beam pipe just outside the ball in symmetrical positions to the interaction region to pick up Bhabhas at small polar angles with a high counting rate due to their steeply rising cross section towards the beam. There are 4 telescopes with scintillation counters to define the acceptance of the monitor followed by a shower counter made of lead-scintillator sandwich. Bhabhas are counted by a coincidence in 2 diagonally opposite counters.

The SAB-luminosity was used in this analysis only to check the Large-angle-Bhabha luminosity (LAB) which was measured by selecting Bhabhas at larger polar angles which hit the NaI of the ball itself. From Figure 6 one can see that the 2 luminosity measurements agree quite reasonably. The ratio between LAB- and SAB-luminosity is 0.97 ± 0.03.

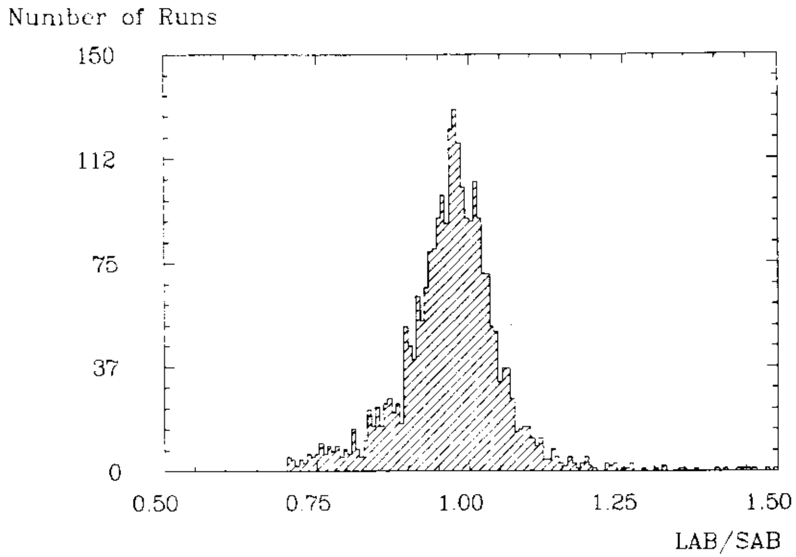

Figure 6. Ratio of LAB- and SAB-luminosity

4.2.6 Time-of-Flight System (TOF)

The Time-of-Flight system did not exist in the SPEAR configuration of the Crystal Ball. It consists of 94 scintillation counters which cover 50 % of the solid angle of the upper hemisphere. They are mounted outside the walls of the dryhouse. The TOF system is needed to distinguish between cosmic ray particles and those originating from the interaction region (e.g. μ-pairs). The counters are equipped to record the position of hits and their relative timing to hits in the ball.

This part of the detector has been used in this analysis to select μ-pairs needed later on to develop cuts on the lateral shower energy distribution (see "Photon Selection") but not for the inclusive γ-analysis itself.

5.0 DATA ACQUISITION

5.1 DETERMINATION OF THE ENERGY DEPOSITED IN A CRYSTAL

The energy deposited in a crystal is proportional to the NaI light output which is recorded by a photomultiplier tube. The resulting analog pulses from the crystals are fed to the CB-control room where they are 'integrated' in the 'Integrate and Hold modules' which hold the charge of the pulses on capacitors until they are consecutively monitored by a 13-bit ADC (Analog to Digital Converter with 8192 channels). This information is read out by an online computer (PDP 11/T55) and then stored on disk or tape. See /CHAN78/ and /CHES79/ for more details on the hardware.

The behaviour of this whole hardware chain should be linear with energy over a wide range (.05 - 6500 MeV). To enlarge the dynamic range each photomultiplier signal is digitized in 2 different channels. The high energy channel (HEC) measures energies in the range 0-6500 MeV whereas the low energy channel (LEC) is amplified by a factor of 20 and covers the energy range of 0 - 330 MeV. If one assumes proportionality,one can relate the measured pulse height H_i and deposited energy E_i by :

$$E_i = S_i (H_i - P_i) \qquad (13)$$

where P_i is the pedestal (the value recorded by the ADC when there was no energy deposited in the crystal) and S_i the proportionality constant (slope) for a crystal i.

In order to completely determine the energy deposited in a crystal one thus has to know 4 constants which are found in a calibration procedure : the attenuation factor (gain ratio) of HEC to LEC,the 2 pedestals and the slope for one of the channels which automatically gives the slope for the other channel using the gain ratio.

5.2 ENERGY CALIBRATION

To ensure stability of the energy measurements and to determine the four above mentioned constants,the crystals are calibrated every 2 weeks (during periods when data are taken) by 3 different methods at 3 different energies :

1. ^{137}Cs-source calibration using photons of E_γ = 0.66 MeV

2. Van-de-Graaff (VdG) calibration using photons from the reaction :

   $$p + {}^{19}F \rightarrow {}^{20}Ne^* \rightarrow {}^{16}O^* + \alpha$$

   where the excited $^{16}O^*$ emits a photon of E_γ = 6.13 MeV. A small Van de-Graaff generator supplies 340 keV protons to excite the Neon resonance /KIRK79/.

3. Bhabha calibration at beam energy (~ 5 GeV)

The first step is to determine the pedestals by studying the pulse heights in a crystal for a small portion of the data sample when no positive signal is seen.

The gain ratios are taken from crystals which had less than 330 MeV deposited energy so that the low energy channel should not overflow.

To complete the calibration it is necessary to measure the slope for either the high or the low energy channel for each crystal. This is done by special calibration runs with t[illegible] Cs-source or the Van-de-Graaff generator when there are no [illegible]ns in DORIS II.

A preliminary estimate of the LEC slope is made by using the 661 keV photon line from a ^{137}Cs-source. For each crystal the position of the photon line in the LEC pulse height spectrum is fitted to determine the slope using Eq.(13) . This results in an energy resolution of about 25 % (FWHM) for the 661 keV γ-line. A second and more accurate determination of the LEC-slopes is made by using photons supplied by the VdG generator.

A significant fraction of the Cs-calibration events deposit almost all of their energy in a single crystal. For higher energies (already for the VdG photons) small amounts of energy leak into neighbouring crystals. So an iterative procedure (starting with the Cs constants) using the sum of the energies in 4 modules instead of only the central one must be used to obtain the slopes. These slopes give an energy resolution of 15 % FWHM at 6.13 MeV.

The final slopes are obtained with the Bhabha calibration. It takes about two weeks (dependent on the performance of DORIS) to collect about 100000 Bhabhas needed to calibrate the detector properly. Here the HEC-slopes are determined. Again leakage into neighbouring crystals has to be taken care of by using 13 crystals to determine the slopes in an iterative procedure. This time the VdG constants are used for the first iteration.

The Bhabha calibration gives an energy resolution of 4.2±1.0 % FWHM at 5014 MeV /MASC84/. If one compares these numbers with the expected resolution of $\sigma(E)/E = 2.7\ \% / \sqrt[4]{E}$ (E in GeV) one notices that it follows the $E^{3/4}$ behaviour but that the resolution is better than expected because one selects only very clean calibration events. Further details on the calibration procedure can be found in /SIEV85/,/MASC84/

However there are important consequences if this calibration procedure assumes a linear relationship between digitized value for the signal and the energy deposited in that crystal using energies far above and below the mean energies usually measured for particles in the ball of about 200 MeV :

1) The invariant $\gamma\gamma$-mass distributions for the π^0 and η (see "Systematic Error on the Energies") are observed to lie systematically lower than their established values /PART84/. The same is true for the mass difference $\Upsilon(2S)$-$\Upsilon(1S)$ in the exclusive cascade transitions

$\Upsilon(2S) \to \pi^0\pi^0 \to \Upsilon(1S)$ and

$\Upsilon(2S) \to \gamma\,{}^3P \to \gamma\gamma\Upsilon(1S)$,where the $\Upsilon(1S)$ decays into 2 leptons /BROC84/

which indicates that perhaps the relationship between pulse height and slope might not be quite as linear as it is parametrized in Eq.(13) .

2) Also the calibration is made for a 2 week running period and fluctuations in the performance of the apparatus on the order of a few hours are averaged over by the Bhabha calibration and probably entirely missed by the Van-de-Graaff calibration which is taken when there are no beams in DORIS II.

One knows this from triggers at random beam crossings which have energies deposited in the ball of typically a few MeV and up to 100 MeV.

What one would like to have to calibrate the NaI in this analysis are photons in the energy range of 100 to 500 MeV. Unfortunately there are no monochromatic γ-sources of this energy available without large efforts.

Additional checks on the stability of the calibration of each module can be obtained by periodically sending pulses of light from a Xenon flash lamp to each phototube via fibre optic cables and a light-emitting diode which is mounted in front of the photomultiplier tube to detect sudden changes in the hardware chain.

5.3 TRIGGER SYSTEM

Every time the electron and positron bunches meet in the interaction region (bunch crossing) it is necessary to make a fast decision if there are e^+e^--annihilation events of a desired type. Therefore a set of triggers is used. The idea is to sum energies (analog pulse heights) from major and minor triangles and decide from these energy sums and/or symmetry and/or multiplicity requirements of combinations of triangles if one wants to further analyze these events.

Two independent systems are used to trigger the experiment in coincidence with the bunch crossing signal. One is composed of compact TTL-,the other of modular NIM-logic. The main triggers used for this analysis are the 'total energy triggers' which have the same requirements for both trigger systems. They sum the pulse heights of all 20 major triangles not counting the endcaps and tunnel modules. Events are accepted if they have more than 1800 MeV total energy. In addition there is a set of triggers which were used to select special physics events like muon pairs,Bhabhas or the exclusive cascade channel $\Upsilon(2S)\to\gamma\gamma ll$ (leptons from the decay of the $\Upsilon(1S)$) which will not be discussed here.

Together with other information about an event like tube chamber hits,different timing signals,triggers etc. the digitized energies are written to tape. These 'raw data' are shipped to SLAC and 'produced' there as explained in the next section.

6.0 PRODUCTION OF DATA

'Production of data' means that individual information like pulse heights from tubes and crystals are used to produce a coherent picture of an event. After a 6 stage 'standard analysis' procedure as described below,the position of hits in the tube chambers and calibrated energies for the crystals are available. Furthermore particles are identified on the basis of the charge information,shape of their shower deposition and energy. Track always refers to a charged or a neutral energy deposition.

These data are then used for the further physics analysis and they are send back to DESY and other collaborating institutions.

6.1 STANDARD ANALYSIS

The 6 different stages of the standard analysis are described in this section under the names used in the offline analysis and described e.g. in /GAIS82/,/HORI84/,/OREG80/, or /RPAR84/.

6.1.1 ENERGY-Step

The energies of all crystals are computed from the pulse heights measured by the ADC. The conversion is done by multiplying with the slope determined by the Bhabha calibration after subtracting the pedestals using Eq.(13).

6.1.2 CONREG Step

CONREG stands for 'Connected Region' (CR) which is a group of crystals touching each other with at least an edge having an energy exceeding a threshold of 10 MeV. A connected region can be seen easily by looking at an enlarged part of a 'Flat Display' of an event (Figure 7). Here the ball is cut along the boundaries of its major triangles and unfolded. Each crystal is projected as a small triangle with the energy inscribed (in MeV).

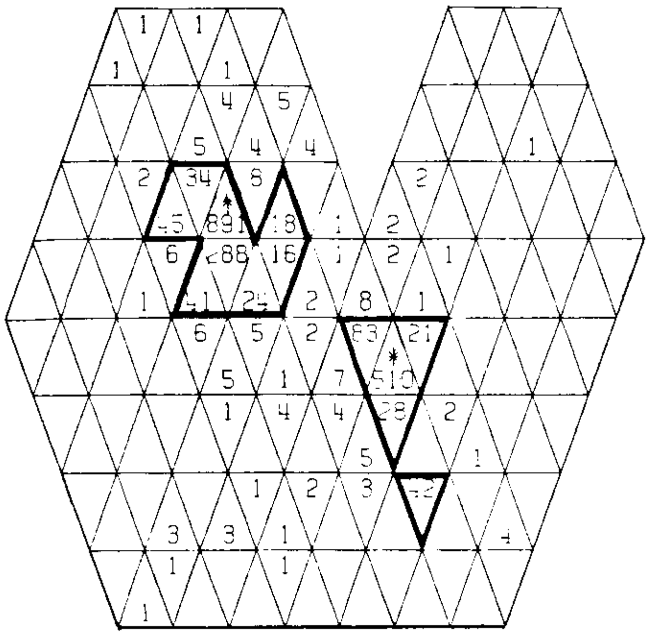

Figure 7. Flat display showing 2 connected regions with the bump module denoted as a *.

6.1.3 BUMPS-Step

A bump is a maximum of local energy deposition in a connected region (see Figure 7). The bump discriminator algorithm determines the number of particles in each connected region. First the most energetic module is picked out and each crystal of that connected region is then tested if it can be explained as a probable shower fluctuation of this 'bump module'. This is done by an empirically found envelope function which depends on the energy of the bump module and the distance between it and the candidate crystal. If all of the crystals of the connected region cannot be flagged as originating from this shower the remaining ones undergo the same procedure until all of them are assigned to a bump.

The discriminator is somewhat biased against finding additional bumps unless there is clearly an excess of energy well separated from the already existing bumps. This bias prevents interacting charged particles which can have irregular shower patterns from creating spurious bumps.

6.1.4 CHGTKS-Step

In this step the tube chamber information is decoded and one tries to find charged particle trajectories not using the information from the ball. These interaction-region-tracks (IR-tracks) fix the z-position of the event vertex assuming x=y=0. In a second stage it 'tags' additional charged tracks by matching hits in the chambers with bumps in the Crystal Ball proper. Any bump which is not caused by a charged particle is assumed to be caused by a photon.

6.1.4.1 Tagging

In this analysis a different algorithm for 'tagging' charged particles is used so that the information from CHGTKS if a track is called charged or neutral is not used. This algorithm tries to find as many charged particles as possible in order to have only clean neutral particles. It uses the information from the tube chamber hits in Φ and z. A χ^2-probability is calculated from the difference in the position from a line connecting the centre of the module in question with the event vertex and the hits in the tube chambers. The total charge probability is the product of the individual probabilities converted into a confidence level for the 6 layers. The range is from 0 to 1, where 1 means most probably a charged track whereas 0 means most likely neutral. A distribution of the tagging probabilities using hadronic events can be seen in Figure 8.

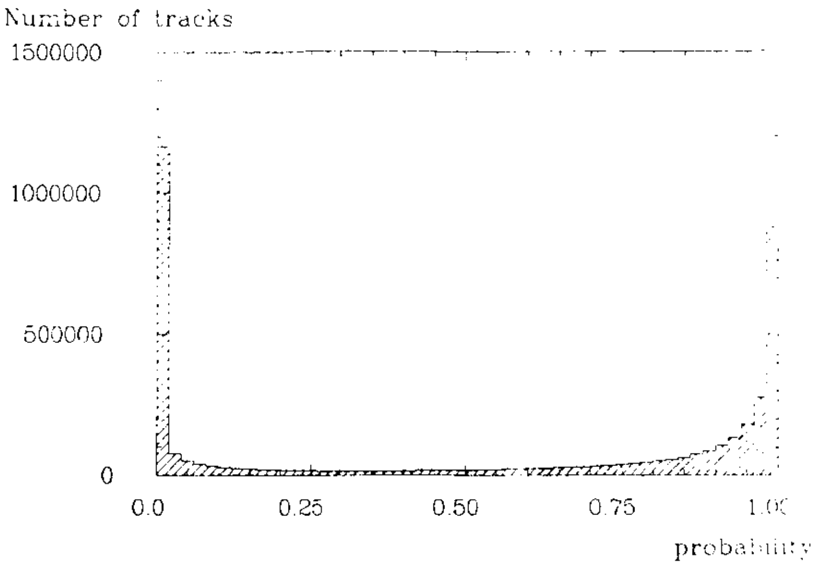

Figure 8. Tagging values for tracks from hadronic events. 0 means most likely neutral, 1 charged. For the inclusive γ analysis a value of less than 0.02 is used to find neutral particles

The decision whether one wants to call a track charged can be varied by using different cutoffs for the charge probability. There are two different ones :

1. The charge probability for a bump module

2. The charge probability for a connected region. It is simply the highest probability from all individual crystals of the connected region.

Unfortunately not all of the charged particles are detected and show up at energies peaking around 210 MeV (punchthrough) with a long tail towards higher energies. Among several reasons there are :

An incorrectly reconstructed z-vertex which is calculated from the chamber hits causing the tracks to tilt so much that they cannot be correlated with an energy deposition anymore

A wide shower from decays of charged hadrons where the point of entry of the primary particle in the ball and the bulk of the deposited energy cannot be associated anymore with each other.

Low efficiency of the tube chambers because of broken wires or amplifiers

To exclude the above mentioned cases in this analysis the charge probability for the connected region is used to make sure that there is no charged track pointing anywhere near the photon candidate.

6.1.5 ESORT-Step

The pattern of an energy deposition contains a lot of information about the direction of a photon. This routine makes use of it to assign measured energies to the different bumps and to find the directions for the neutral tracks. For this purpose the bump module is subdivided into 16 hypothetical submodules. The observed energy distribution in the bump module and its neighbouring crystals is compared to an expected distribution assuming that the photon impacted at this submodule centre. In an iterative procedure the submodule which minimizes the difference between observed and expected energy distribution is found for that bump and the direction cosine for this submodule will then be used as the direction of the photon. Using this or similar methods the Crystal Ball has achieved an angular resolution for photons of σ = 30 - 50 mrad with a slight energy dependence [GAIS82].

6.1.5.1 Energy of a Cluster

The energy of a particle is determined in this analysis by using the E13-algorithm($\sum$13) instead of ESORT. It uses the fixed pat tern of 12 crystals surrounding the bump module as can be seen in Figure 9. In some cases where the bump module is at a major triangle vertex only 11 additional crystals are involved.

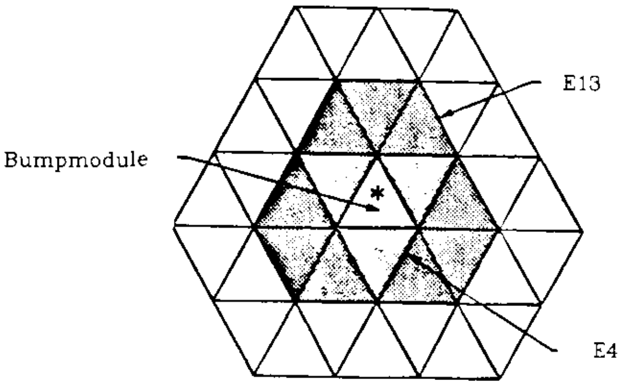

Figure 9. Summing conventions for E1,E4 and E13=$\sum$13

This method does not try to unscramble overlapping showers as ESORT does (see /RPAR84/for ESORT). It is therefore much simpler and does not need shower functions and fine tuning of parameters which depend on the environment of the cluster in question. E13 systematically underestimates the energy of electromagnetic showers by neglecting $\sim$ 2.2 % of energy distributed outside the $\sum$13. On the other hand it overestimates energies if two bump modules are too close to each other so that the E13-energies overlap and some energy is counted more than once. To prevent energies being shared by more than one particle in the selection of the inclusive photon spectrum an overlap cut of 30 ° is used.

Another correction is the position correction which adjusts the energy by estimating the impact of a particle in a crystal relative to the centre because showers near the centre have a better light propagation in the crystal than those near the edges of

crystals due to loss of light in the paper which optically isolates the crystals from each other.

Using this algorithm an energy resolution of $\sigma(E)/E = 2.7\ \% / \sqrt[4]{E}$ (E in GeV) is achieved for clearly separated photons in a hadronic environment.

6.1.6 TFANAL-Step

This step is new for DORIS II data as it produces the information for the Time-of-Flight system. It computes the position of hits in the counters and the time difference between the bunch crossing and hits in the counters. Then it tries to match tracks with these hits.

7.0 HADRONIC EVENT SELECTION

For the inclusive photon analysis one uses hadronic events which make up the major part of the decays of the $\Upsilon(2S)$,$\Upsilon(1S)$ and ^3P_J states. Unfortunately most of the triggers on raw data tape are not of that type. As one can see from the total energy distribution in Figure 10 for the final sample of hadronic events and for one raw data tape,only ~ 2 % of all taken triggers are hadronic events.

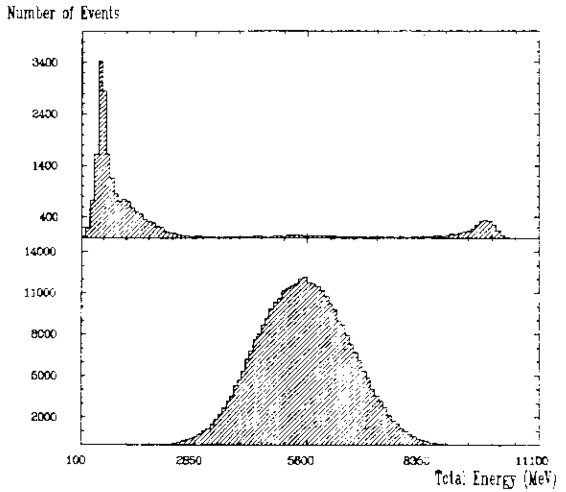

Figure 10. Total energy distribution for all triggers from 1 raw data tape (top) compared with the distribution for the final hadron sample

One can see a lot of high energetic events around 10 GeV corresponding to Bhabhas and the main part of the triggers towards the low energetic side of the distribution which are mainly cosmics and beam-gas events. Hadrons are found between these two dominant peaks.

The main sources of background are cosmic muons,QED-events like $e^+e^- \to \mu^+\mu^-(\gamma)$,$e^+e^-(\gamma)$,$\gamma\gamma(\gamma)$, $\tau^+\tau^-(\gamma)$,two photon events and of course beam related background like beam-gas and beam-beam pipe interactions. Most of these background sources can be removed by energy,multiplicity and/or symmetry requirements for an event as done in the hadronic event selection process. Small contributions due to $\tau\tau$-events with higher multiplicities are hard to remove as they look very similar to hadronic events.

A non-removable background are hadronic events produced in non-resonant production which cannot be separated from the hadronic decays of a resonance.

The original hadron selection program which has been used in the ψ-energy region /GAIS82/ was scaled to Υ-energies but for DORIS II running there were additional problems which were not so crucial for SPEAR data taking : The beam related background was much higher and harder to identify due to higher currents in the machine. Another difficulty for the $b\bar{b}$ resonances is that the ratio of hadronic decays from resonance and continuum is reduced by at least a factor of 35. For the $\Upsilon(2S)$ the signal to background ratio is about 1 : 1 and for the $\Upsilon(1S)$ roughly 3:1 as can be seen in Figure 11.

So in a another selection one tried to isolate hadronic decays with as few background events as possible. This lowered the efficiency to select hadronic events compared to the above mentioned program slightly but also removed a sizeable amount of beam related background.

The selection programs were developed and tuned mainly by looking at separated beam data which are taken when the electron and positron beams are separated by a small distance so that they do not collide in the interaction regions. From these data one expects only beam related background and cosmics.

The hadronic events are identified in the production process and flagged to be written to special tapes later on.

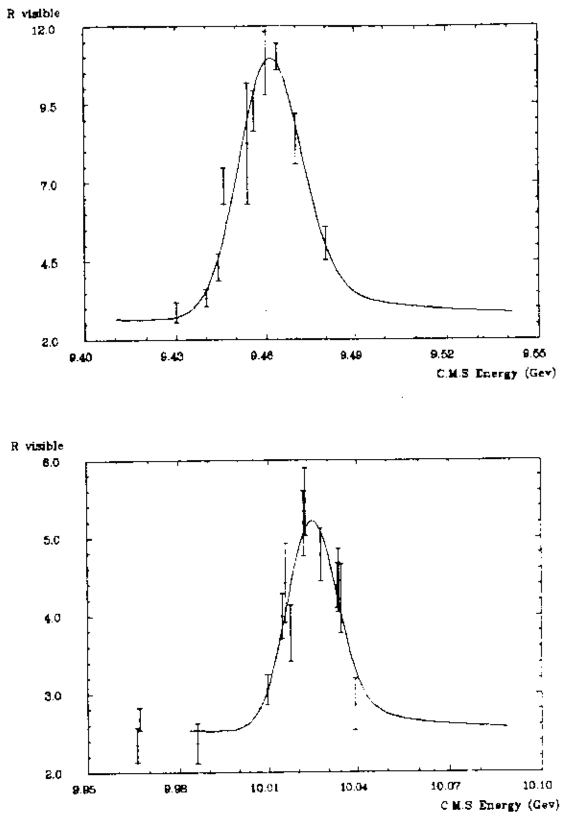

Figure 11. Typical resonance curves for the Υ(1S) and Υ(2S) resonance (bottom). The drawn curves are Gaussian line shapes with radiative corrections /JACK75/ to determine the energy of the resonances

---

Discussed below is the hadron selection program developed for DORIS II running. The following cuts to select hadronic events can already be done after the ENERGY step :

1. The total measured energy in the ball including the endcaps should be more than 10 % of the centre of mass energy.

This cut especially removes cosmics and μ-pair events which deposit typically 200 - 500 MeV in the ball as they are mainly minimum ionizing particles.

2. The ratio of energy in the tunnel crystals compared with the energy in the whole ball should be less than 50 % and the ratio of endcap energy to the total energy should be below 40 % .

   The energy measurement in those regions of the detector is not very reliable as there are only a few radiation lengths of NaI in the endcaps.

   This should remove beam related background events which generally have large energy depositions in directions close to the beam.

3. A very effective cut in removing beam related and cosmic ray events is a 2-dimensional cut in the vector energy sum $\vec{\beta}$ and the transverse energy E_{trans} of an event. $\vec{\beta}$ is defined as

$$\vec{\beta} = \sum E_n \vec{r}_n \; / \; E_{Ball} \qquad (14)$$

As the Crystal Ball cannot measure momenta of particles, energy vectors are used by summing over the energies E_n of all existing crystals n of the ball using the unit vector $\vec{r}_n$ of the centre of the module to determine the direction. This sum is normalized to the total observed energy in the ball E_{Ball}. If all the particles were photons or electrons and all of their energy were deposited in the ball this vector sum should be 0 due to energy and momentum conservation.

The transverse energy E_{trans} is the sum of the absolute values of the energy vectors projected into the x-y plane (transverse to the beam) and normalized to the c.m.s. energy $\sqrt{S}$.

$$E_{trans} = \sum E_n \sin\Theta_n \; / \; \sqrt{S} \qquad (15)$$

The usefulness of this cut can be seen in Figure 12 which shows the removal of beam related and cosmic ray backgrounds with the cuts indicated by comparing separated beam and colliding beam data.

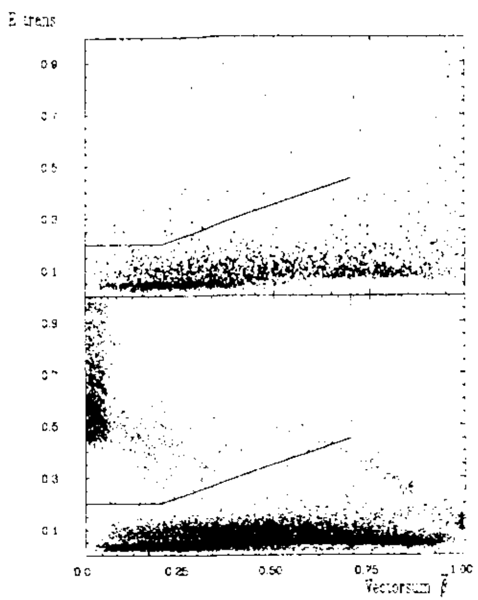

Figure 12. Transverse Energy against vectorsum $\vec{\beta}$ of an event: On top is the distribution for separated beam data,on the bottom for colliding beam data.The cuts used are indicated as lines.

The following cuts are used to discriminate against high energetic QED background like Bhabhas and real $\gamma\gamma$-events and can be made after the CONREG- or BUMPS-stages.

The requirements are :

4. There should be at least 4 connected regions . Bhabhas typically have 2-4 connected regions but only a few radiative ones have

5. more than 3 connected regions with more than 100 MeV in the ball.

To further reduce the background especially of radiative QED events one requires that :

6. at most one connected region may have an energy greater than 80 % of the beam energy but if there is one, the total energy in the ball should be less than 75 % of the centre of mass energy

7. The last requirement is that there must be at least 3 bumps in the ball within $\cos \Theta_i < 0.85$.

It should be noted that no information from the tube chambers is used in this hadronic event selection and that only candidates which survive this selection process will be further investigated for the inclusive photon analysis.

An example of a flat display of a hadronic event is displayed in Figure 13. One can see the hexagonal openings in the tunnel regions where the energies deposited in the endcaps are indicated and a rather symmetric pattern for the deposited energies clustering in certain areas of the ball.

The hadronic data samples used for this analysis contain all data taken until the end of February 1984. The number of events and luminosities are listed in table 1.

C.M.S. Energy (GeV)	Hadrons / 1000	Luminosity (pb^{-1})	Resonance / 1000
$\Upsilon(1S)$ (9.46)	104.1	10.2	88.5 ± 6.7
$\Upsilon(2S)$ (10.02)	338.2	60.6	193.5 ± 15.5
9.98	13.1	4.6	----------

Table 1. Luminosity and number of events used for this analysis

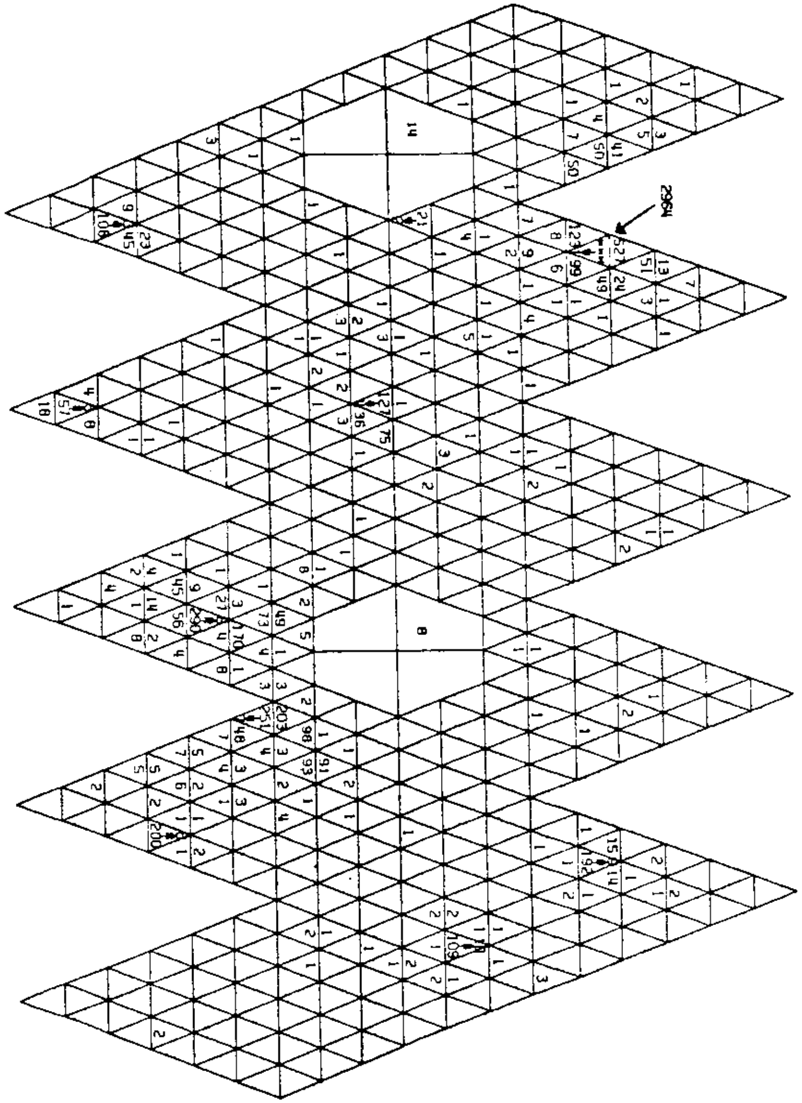

Figure 13. Flat display of a hadronic event

7.1 HADRON SELECTION EFFICIENCY

In order to evaluate the overall hadronic event selection efficiency ε_{had} and the number of produced resonance decays, Monte Carlo events were generated according to the following channels:

$\Upsilon(2S) \rightarrow \gamma\,^3P_J \rightarrow \gamma$ + hadrons

$\Upsilon(2S) \rightarrow$ 3 gluons $\rightarrow$ hadrons

$\Upsilon(1S) \rightarrow$ 3 gluons $\rightarrow$ hadrons

$\Upsilon(1S) \rightarrow q\bar{q} \rightarrow$ hadrons

where all known branching ratios and cross sections for the resonances and continuum are incorporated. The 3-gluon decay was modelled by an improved version of the LUND-model /SJÖS84/. Hadronic as well as electromagnetic interactions between the final state particles and the detector material are simulated by the High-Energy-Transport Code (HETC) /GABR81/ and the Electron-Gamma-Shower program (EGS) /FORD78/.

The hadron selection efficiency for the decays of the $\Upsilon(2S)$ was determined to be ε_{had} = 86 ± 7 %.

7.2 NUMBER OF RESONANCE DECAYS

The number of produced hadronic events from the resonances N_{res} is obtained by taking the found number of events N_{had}, subtracting the number of continuum events and correcting this number for the above selection efficiency ε_{had}. The number of continuum events is calculated from the data taken in the nearby continuum (9.98 GeV). N_{cont} is scaled to the full resonance sample using the cross sections for hadron production at the different beam energies E_{res}, E_{cont} and the different Large-angle-Bhabha luminosities $(LAB)_{cont}$,$(LAB)_{res}$. The final number of resonance decays is then calculated using the formula :

$$N_{res} = \left(N_{had} - N_{cont} \frac{(LAB)_{res} E^2_{cont}}{(LAB)_{cont} E^2_{res}} \right) \frac{1}{\varepsilon_{had}} \qquad (16)$$

The numbers used for this analysis can be found in table 1.

7.3 RESONANCE SCAN

Another application for the hadron selection program is to scan the resonance peaks carefully before each major data taking period to be sure that one is measuring at the beam energy which corresponds to the peak of the resonance and therefore to the best ratio of resonance to continuum production. For this purpose the R value was calculated using Eq (7). The 'visible' R is not corrected for the hadron selection efficiency. Typical measured values of $R_{visible}$ are plotted for the $\Upsilon(2S)$ and $\Upsilon(1S)$ resonances as a function of the DORIS c.m.s. energy in Figure 11.

During the run the stability of the R value is monitored and can be seen in Figure 14 where this value is plotted against the run number which can also be interpreted as a time scale.

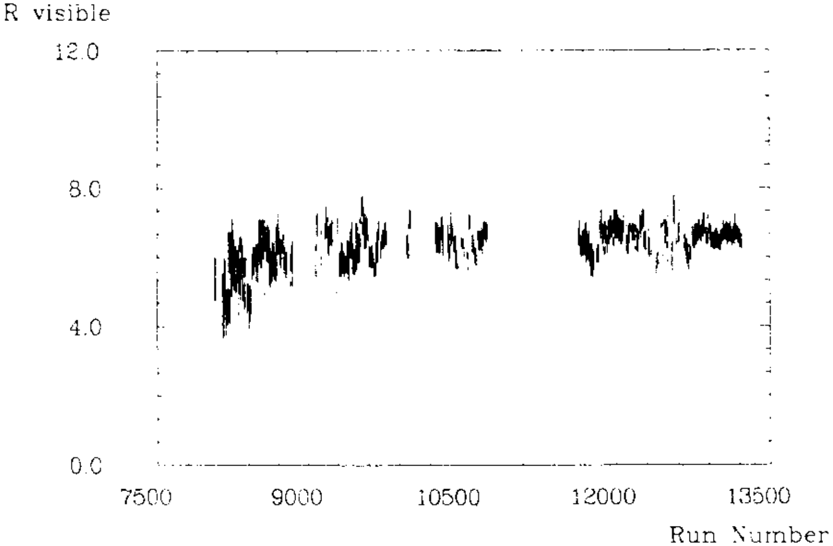

Figure 14. The uncorrected R value as a function of the run number. 5 runs are always combined.

The observed small fluctuations in R probably indicate that the beam energy of DORIS II was not always exactly at the value corresponding to the peak of the $\Upsilon(2S)$ resonance.

8.0 PHOTON SELECTION

One of the main goals of the data taking at DESY was to find monochromatic photon lines corresponding to transitions between different $b\bar{b}$ states as indicated in the level scheme in Figure 1 on page 3. In order to select clean photons in a complicated hadronic environment, one has to apply certain cuts. The idea is to remove any particle from the spectrum which is not neutral,is too close to another one, reconstructs with another photon to a π^0 or does not satisfy the typical shape of a photon shower. In the end there should only be photons clearly separated from any other energy deposition to give the best possible energy resolution. The cuts which lead to the final inclusive photon spectrum will be described in the following.

A photon candidate has to fulfil the following criteria :

1. No charged track should point to the connected region which makes up the cluster in question. The charge probability (as defined in "Tagging") for the connected region should be less than 2 %.

   Hadronic interactions sometimes produce showers which are far from their original entry point in the ball and from a possible charged track in the tube chambers. Therefore all crystals in a connected region which could contribute to the shower are checked if they have a charged track pointing towards them.

   One can see from Figure 15 which shows the spectrum before and after the cut and the rejected part that the peaking of the spectrum around 210 MeV which corresponds to minimum ionizing particles is sharply reduced.

   All plots of γ-spectra are plotted on a logarithmic energy scale to take into account the $E^{3/4}$ dependence of the resolution. The binning is always $\Delta(\ln(E))$=3 % for an energy E (in MeV).

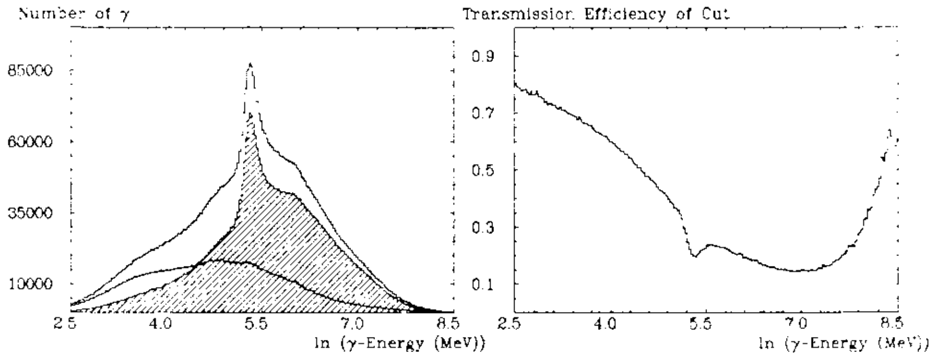

Figure 15. Spectrum before and after the first cut (neutral requirement). On top (left) is always the spectrum before the cut,shaded is the rejected part and the second line with the error bars corresponds to the spectrum after the cut.The plot on the right shows the transmission efficiency (number of particles per energy bin surviving the cut divided by the number before the cut). All plots have a logarithmic energy scale with a binning of $\Delta(\ln(E))$ = 3 %.

2. The candidate has to be in the limited solid angle which is covered by all 3 chambers,i.e. $|\cos(\Theta)| < 0.75$. From Figure 16 it can be seen that outside the coverage of the outer chamber the number of neutral particles starts to increase because some of the charged tracks could not be correctly identified as being charged by the inner 2 chambers by themselves.

   The spectrum before and after the cut is shown in Figure 17.

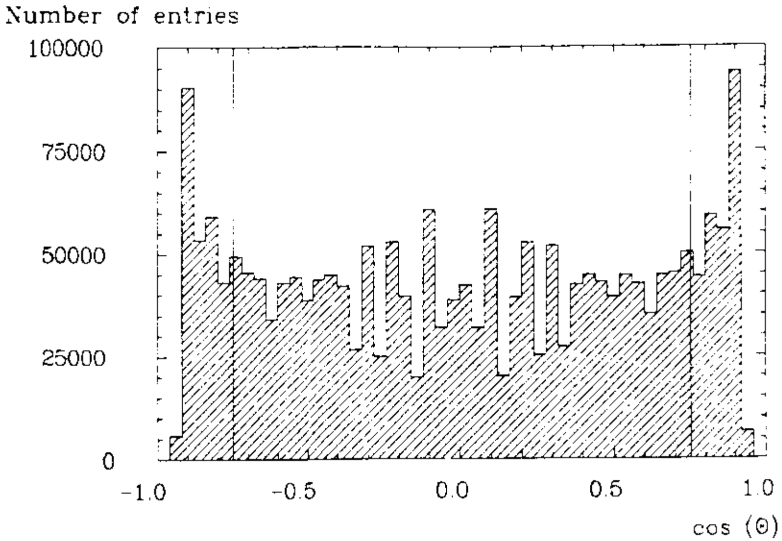

Figure 16. cos(Θ)-distribution for neutral particles with the cuts indicated at ± 0.75

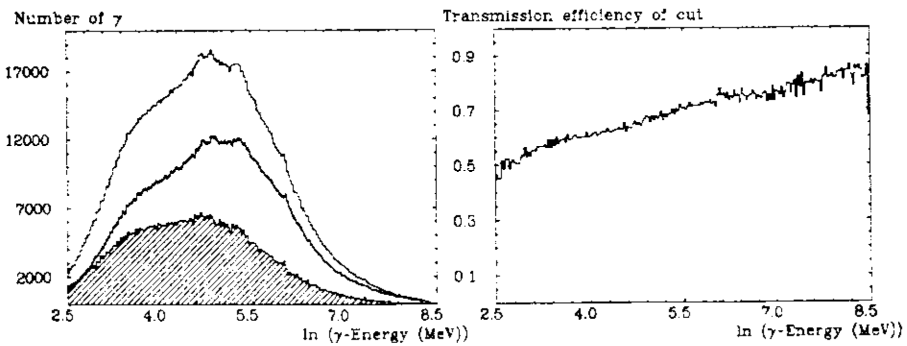

Figure 17. Spectrum before and after cos (Θ) cut

3 The photon candidates have to pass a 'pattern cut' to ensure that showers have a certain shape which is compatible with that of a photon (For a graphical comparision of the typical shower deposition patterns by looking at enlarged parts of a flat display for photons and the particle types described in the following see Figure 18). The main purpose of the pattern cut is to reject :

Minimum ionizing particles which were not recognized by the tube chambers (punchthrough) which typically deposit their energy in 1 or 2 crystals (Figure 18a);

Interacting hadrons. They have broad and very irregular shower deposition patterns (Figure 18b);

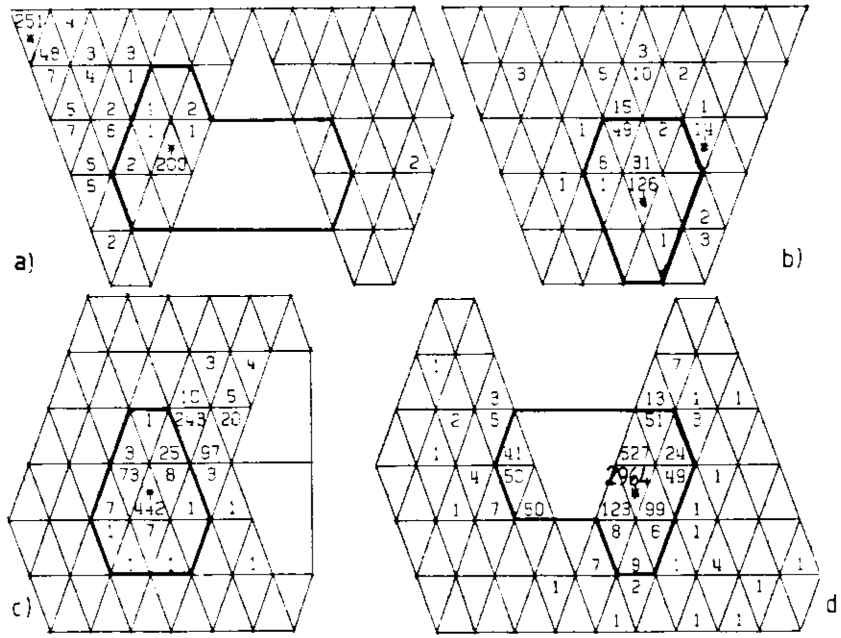

Figure 18. Typical shower deposition patterns as described in the text in comparision with a photon (d). Indicated are the 13 modules which determine the energy.

Overlapping photon showers (e.g. from 2 merged photons resulting from a π^0 decay) (Figure 18c).

Pattern cuts compare the ratio of energies in different parts of the shower. E1 is the energy of the bump module, E4 and E13 are summations of energies as can be see from Figure 9. In this analysis cuts on E1/E4 and E4/E13 are used. These cuts separate minimum ionizing particles from photons as one can see in Figure 20 which shows a comparision of these variables for muon pairs produced in the QED reaction $e^+e^- \rightarrow \mu^+\mu^-$ and Monte Carlo generated photons with the cuts indicated. For minimum ionizing particles the ratios are very close to 1 while for photons which typically spread over 13 crystals the ratios are lower.

One can see from the rejected spectrum and the transmission efficiency (Figure 19) that a lot of low energy particles are removed which correspond to hadronic interacting particles or at least parts of them found as a separate bump. Some more particles in the region around 210 MeV are rejected and also a lot around E=1000 MeV (ln(E) = 7) corresponding mainly to merged photons from a π^0.

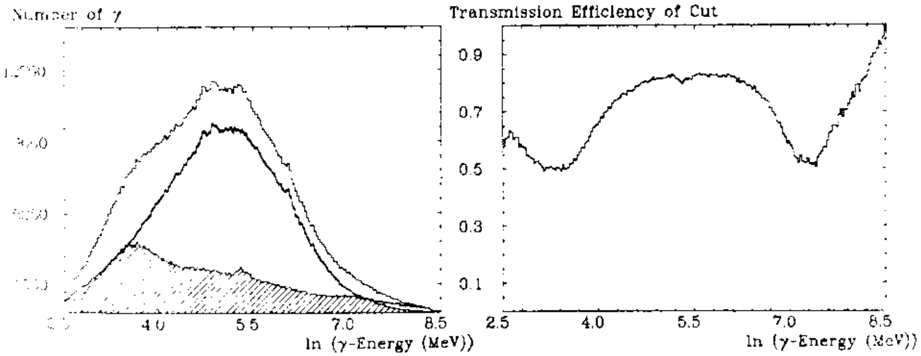

Figure 19. Spectrum before and after pattern cut

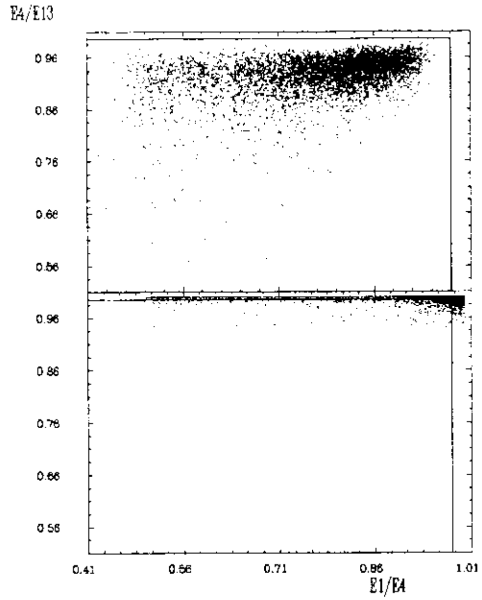

Figure 20. Pattern cut used to reject punchthrough. The lower plot shows μ-pair events,the upper plot Monte Carlo generated photons.The used cuts are indicated as lines.

4. The next set of cuts tries to isolate the photon in question from other particles and remove showers which could be caused by hadronic interactions or 2 merged photons from a π^0 by requiring :

There should be no other particle within 30 °.

In addition there should be only one bump in a connected region.

The ratio of the E13-energy and the energy in the connected region should be larger than 1.

One only wants to have showers which do not extend too far outside the 13 (12) modules which are used to determine the energy. This again is a pattern cut but here it removes clusters which are too wide spread and therefore incompatible with the shape of electromagnetic showers.

After these cuts one can see (Figure 21) that a lot of the γ-candidates are removed which have energies greater than 500 MeV corresponding mainly to partly merged photons resulting from a π^0-decay.

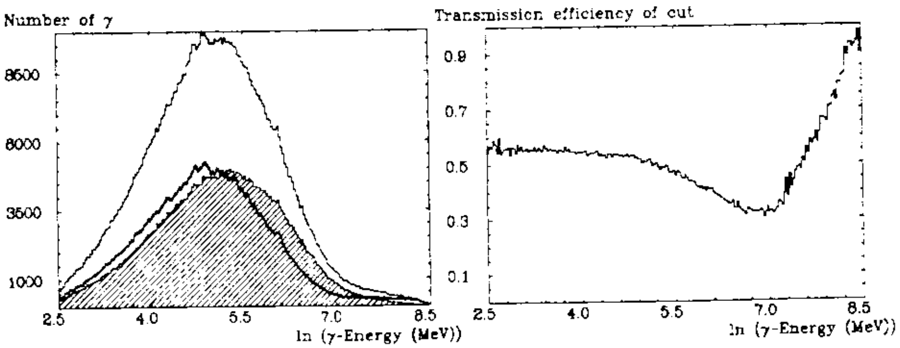

Figure 21. Spectrum before and after separation cut

5 The last cut removes photons which can be explained as the partner of another photon (defined by the above cuts) from the decay of a π^0.

A search algorithm calculates the invariant mass of each possible pair of photon candidates using the directions, energies and their errors. A fit is made to a π^0 mass hypothesis and a χ^2 probability from the fit is calculated. All pairs surviving the χ^2-cut are then used in a search which finds the maximum number of pairs (configuration) in the event using each photon at most once. The configuration is accepted if the confidence level based upon the total χ^2 of the pairs is greater than a minimum value. As can be seen from the invariant mass distributions of 2 photons in Figure 22 before and after π^0-subtraction, this algorithm also removes combinations of photons which did not actually belong to a π^0 decay so that there is also some loss in the inclusive γ signals due to wrong combinations.

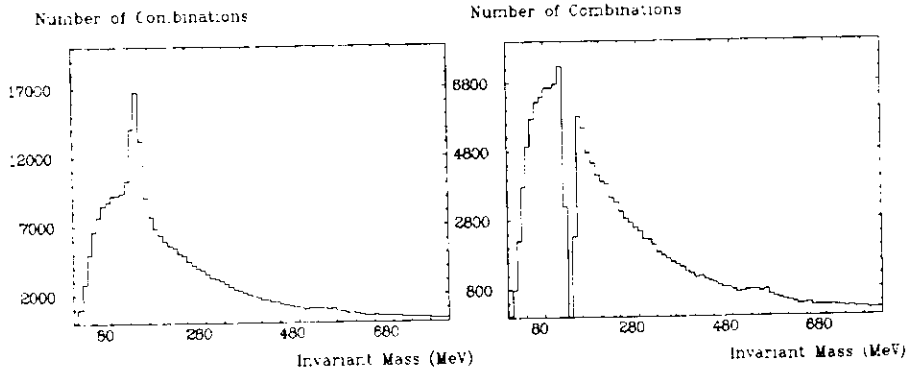

Figure 22. Invariant mass spectrum of 2 photons before (left) and after (right) π^0-subtraction

The reduction of the photons in the spectrum by the π^0-subtraction is shown in Figure 23.

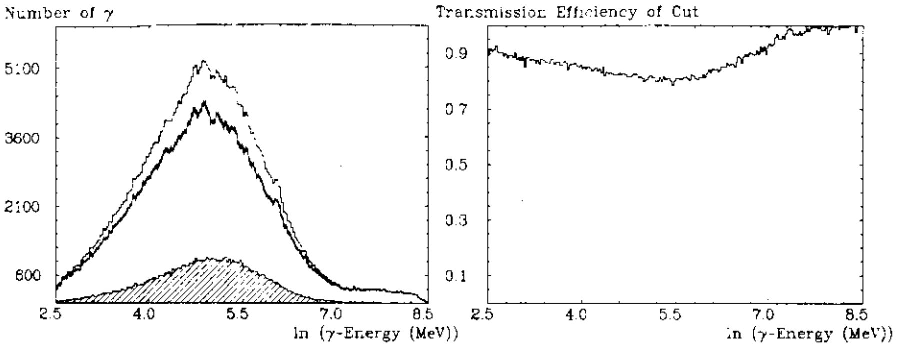

Figure 23. Spectrum before and after π^0-subtraction

9.0 FINAL INCLUSIVE γ-SPECTRUM

One can see how after succesive cuts 3 lines start to show up (Figure 25) in the region 100 - 165 MeV and another one around 420 MeV.

The final spectrum after all cuts is shown again with an enlarged scale in Figure 24.

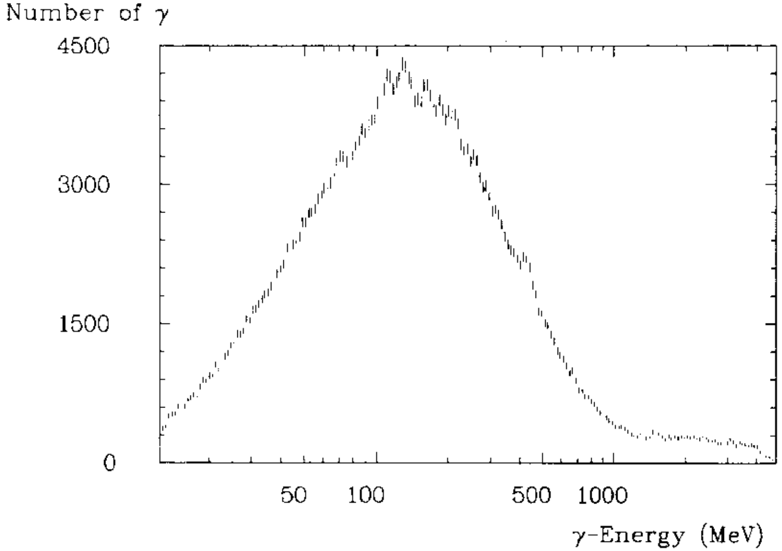

Figure 24. Inclusive γ-spectrum after all cuts

In order to extract the means,amplitudes and significances of the lines from the spectrum a fit was performed. This can be made in 2 different ways :

One fits only a small portion of the whole spectrum in the energy range around the signal in question ('local' fit) as can be seen in Figure 26 before and after background subtraction. The same fit is done for a spectrum plotted on a

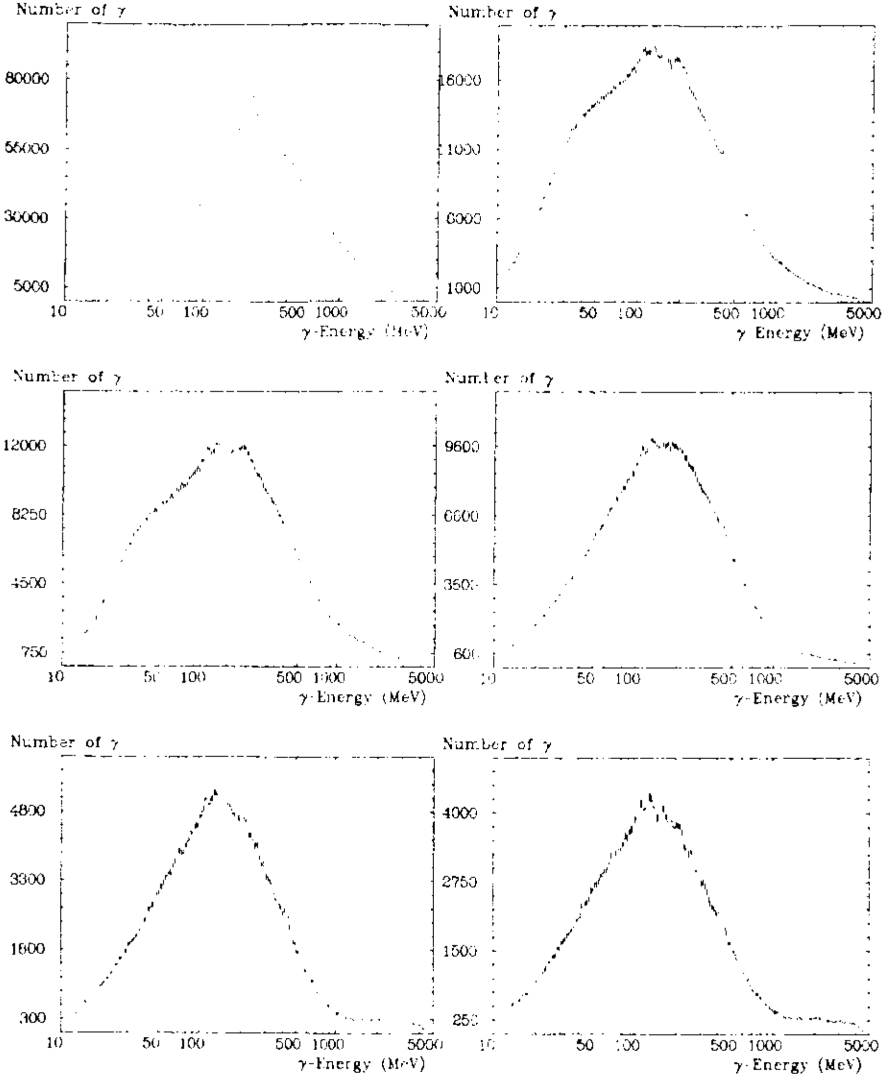

Figure 25. Inclusive photon spectrum after successive cuts. The plots correspond to the spectra before any cut (upper left) and after successive cuts from left to right and from top to bottom following the order in the previous chapter.

linear energy scale (same figure). This is modelled by a smooth background of Legendre polynomials with 3 gaussian line shapes for the 3 lines in the region of 100 - 165 MeV. Due to the closeness of the line around 160 MeV to the punchthrough region the result of this method is very much dependent on the fit window used.

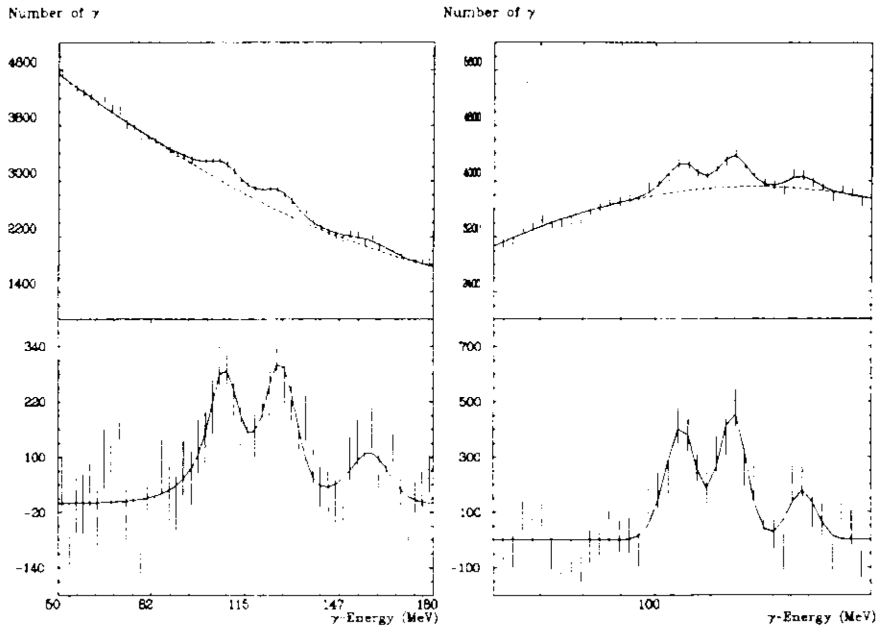

Figure 26. Local fit to the inclusive γ-spectrum before (top) and after background subtraction (bottom). The right spectrum is plotted on a logarithmic, the left one on a linear energy scale.

The results of the local fit can be found in table 2 for the spectrum plotted on a linear and the one on a logarithmic energy scale.

Linear Energy Scale (MeV)	Logarithmic Energy Scale (MeV)
107.4 ± 0.9	107.9 ± 0.8
127.0 ± 0.9	127.1 ± 0.8
157.8 ± 1.9	158.5 ± 1.9

Table 2. : Results for the local fit plotted on a linear and a logarithmic energy scale.

This method was used only to check the second method which is to

perform a 'global' fit to the whole spectrum which necessarily requires a detailed model of the background taking into account contributions from misidentified charged particles and the broad photon background.

This method was used to find the final values for the energies and branching ratios for the seen lines and will be described in more detail in the following

The spectrum was fitted from 55 - 670 MeV using the sum of the following terms:

1. A smooth fourth order Legendre polynomial series representing the photon background.

2. A charged particle spectrum with variable amplitude to take into account the remaining 'punchthrough' of charged particles. This spectrum is obtained by taking genuine charged particles as defined by the three tracking chambers and applying the same cuts as in the photon selection.

3. Three Gaussian distributions with their widths fixed to the known energy resolution of $\sigma(E)/E = 2.7\,\% / \sqrt[4]{E}$ (E in GeV) to describe the signals in the 100-165 MeV region. It is

assumed that the detector's resolution entirely dominates the natural line shape of these lines so that they can be described by a gaussian.

4. Two gaussian distributions to describe the Doppler broadened lines around 420 MeV, at energies fixed by the two lower energy lines and the known $\Upsilon(2S)$- $\Upsilon(1S)$ mass difference of 563.1 ± 0.4 MeV.

This is the mass difference of the weighted averages of the $\Upsilon(2S)$ and $\Upsilon(1S)$ mass as can be seen in table 3 where the masses of precision measurements are given.

Storage ring		$\Upsilon(1S)$	$\Upsilon(2S)$
VEPP-4	/ARTA82/	9459.7±0.6	-------
VEPP-4	/ARTA84/	9460.6±0.4	10023.8±0.5
DORIS II	/BARB84/	------	10023.1±0.4
CESR	/MACK84/	9460.0±1.3	------

Table 3. : Masses for the $\Upsilon(1S)$ and $\Upsilon(2S)$ resonance

It is assumed that the structures around 108,128 and 158 MeV are due to the transitions $\Upsilon(2S)\to\gamma 1^3P_2$, 1^3P_1 and 1^3P_0 respectively and that the line around 420 MeV is only due to $1^3P_{2,1}\to\gamma\Upsilon(1S)$ decays. The model dependence for the secondary lines has no influence on the measurement for the low energy lines. Only two daughter lines are included in the fit as the $^3P_0$ state is expected to have a small $^3P_0 \to \gamma\Upsilon(1S)$ branching ratio /NOVI78/. This is indeed shown in studies of the exclusive channel $\Upsilon(2S) \to \gamma\gamma\Upsilon(1S) \to \gamma\gamma l^+l^-$ by CUSB /PAUS83/ and the Crystal Ball/BROC84/ by the absence of a third line corresponding to that transition. The Doppler shift in the secondary lines is also included.

The fit determines the following parameters:

1. the peak energies of the three low energy lines,

2. the amplitudes of all lines,

3. the coefficients of the Legendre polynomial series.

4. the amplitude of the residual charged particle background.

The result of a fit to the inclusive photon spectrum is shown in Figure 27.

The quality of the fit is good, having a χ^2 per degree of freedom (71 d.o.f.) of 1.05. The percentage for the charged particle background of 3.35 ±0.79 % agrees with the method described later on in "Another Method to determine the Punchthrough" of 2.64 ± 0.75 %.

The results for the global fit are listed in table 4 where only the statistical error is given together with the significances of the lines taken from the number of photons in the peaks.

The systematic errors are discussed in "Systematic Error on the Energies."

Energy (MeV)	Significance
108.0 ± 0.7	8.3 s.d.
127.5 ± 0.7	10.4 s.d.
158.7 ± 1.5	5.5 s.d.

Table 4 : Results for the global fit and the significances of the lines in standard deviations taken from the measured amplitudes.

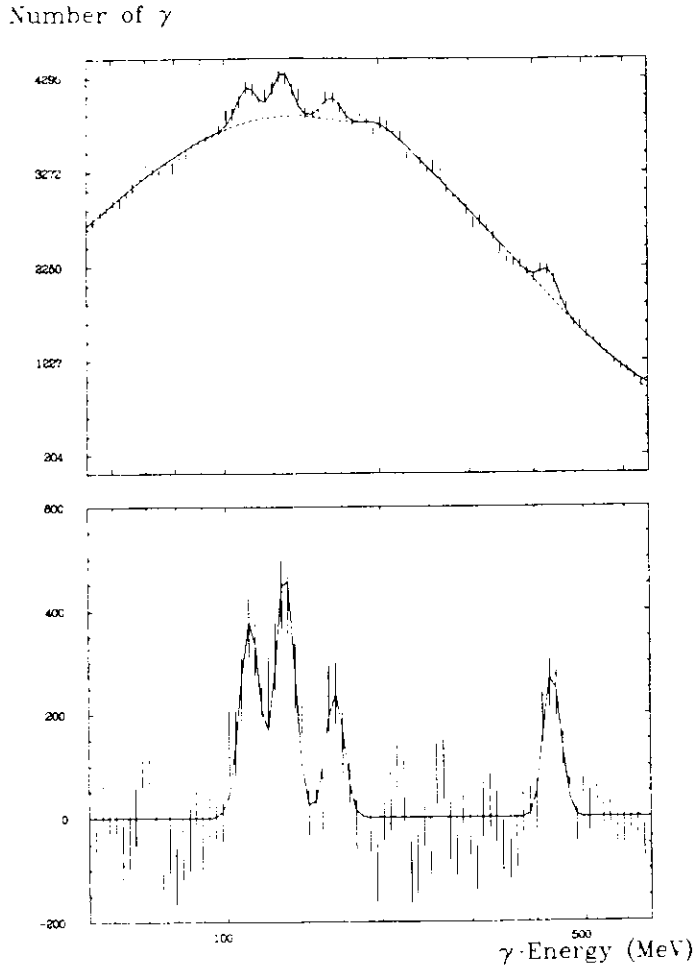

Figure 27 Fit to spectrum before(top) and after background subtraction (bottom).The dotted line in the upper plot represents the smooth polynomial background. The charged particle 'punchthrough' background is given by the difference between the dashed and the dotted line. In the lower figure these backgrounds have been subtracted.

9.1 ENERGY CORRECTIONS

The π^0-search algorithm (see "Photon Selection") determines the π^0- and η-masses from their decay into 2 photons. It was found that the 2 masses are lower than their established values /PART84/ by 1.9 and 3.3 % respectively. This can be corrected by using an energy correction as explained below.

The π^0-mass is found by fitting the curve resulting from all photon-photon combinations which are used to find π^0's as can be seen from Figure 22 with a gaussian line shape over a smooth background of Legendre polynomials (Figure 28). The π^0 mass was determined to be 132.53±0.14 MeV.

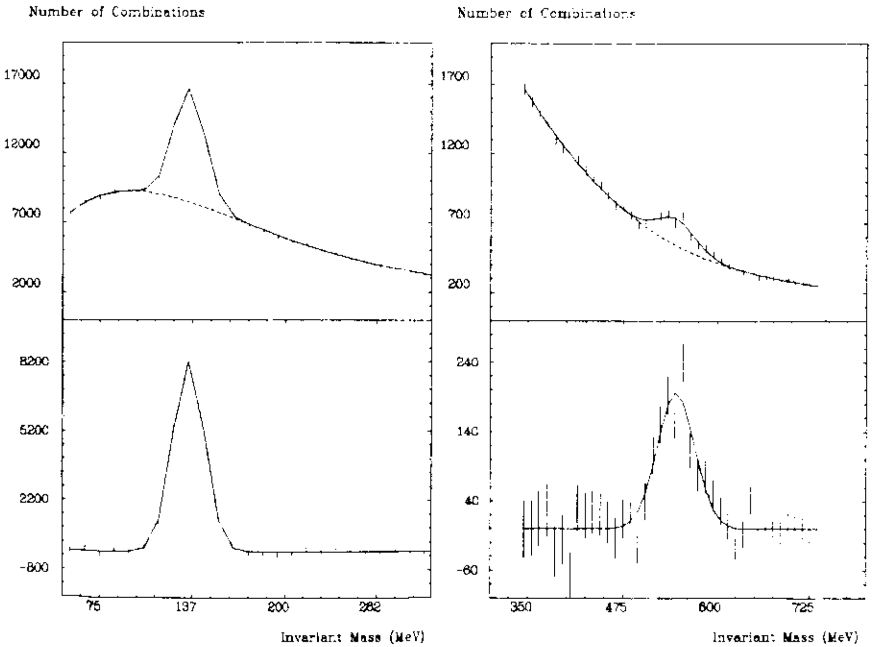

Figure 28. Fit to π^0(left)- and η-mass(right) before (top) and after background subtraction

The η-signal is buried under a combinatoric background caused by incorrect pairings of π^0 photons. To determine the η-mass all combinations of photons where at least one of them had already been used in the reconstruction of a π^0 were removed. One can see an η-peak (Figure 28) which was fitted in the same way as the π^0-mass. The η-mass was determined to be 531.18±2.17 MeV.

One should note that for the determination of the invariant masses not only the errors in the energy scale are important but also the errors in measuring the photon directions.

It was also noticed in the global fit to the inclusive photon spectrum that by varying the mass difference for the $\Upsilon(2S)$-$\Upsilon(1S)$,the quality of the fit could be improved as can be seen by plotting the χ^2 distribution versus the mass difference in Figure 29

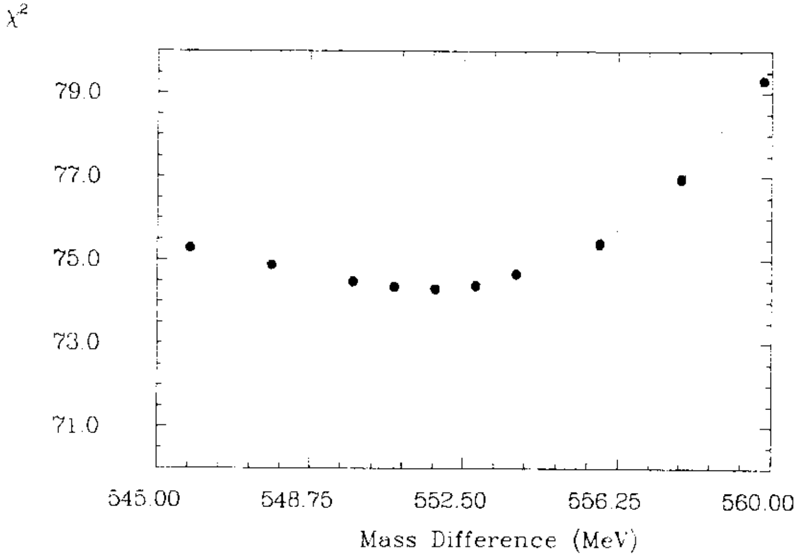

Figure 29. χ^2-distribution for the mass difference $\Upsilon(2S)$-$\Upsilon(1S)$

The χ^2-distribution suggests a value of 551.5 ± 5.5 MeV which is 2.1 % low compared to the experimental measurements (table 3).

9.1.1 Energy Correction for Exclusive Channels

An empirical energy correction was applied for the exclusive transition :

$\Upsilon(2S) \to \gamma\gamma l^+ l^-$, leptons from the decay of the $\Upsilon(1S)$

such that the mass difference $\Upsilon(2S)$-$\Upsilon(1S)$ corresponded to the established value /PART84/

The correction is of the form :

$$E_{corrected} = \frac{E_{measured}}{(1-\alpha \, \ln(E_{measured}/E_{beam}))} \qquad (17)$$

with α being a constant to be determined. This form of correction is used as it takes into account the logarithmic shower dependence and the fact that at the beam energy the correction must be 0 as Bhabhas are used for energy calibration.

This correction was then used to check the π^0-mass in the transition

$\Upsilon(2S) \to \pi^0\pi^0 l^+ l^- \to \gamma\gamma\gamma\gamma \, l^+ l^-$, where the leptons define the decay of the $\Upsilon(1S)$.

The π^0-mass was found to agree /BROC84/ with the established value. The correction factor α found in this way is very depend-ent on the cuts used and is only valid for very clean photons,e.g. the final photons in the inclusive analysis or exclusive low multiplicity events.

9.1.2 Energy Correction for the Inclusive γ Analysis

After this success for the above mentioned exclusive channels one also tried to use the correction for the inclusive photon analysis. But using the same constant determined by the exclusive analyses the masses of π^0 and η came out far too high.

In the inclusive photon analysis one noticed that by merging photons into hadronic events of the $\Upsilon(1S)$ and $\Upsilon(2S)$ to determine

the detection efficiency (see "Photon Detection Efficiency") the energy always came out higher by a mean value of 3.5 MeV once they were merged into a real event. This might be explained by hadronic debris in the event which added to the merged photon energy. The energy correction takes this into account and subtracts 3.5 MeV from the photon energy before applying the correction as mentioned above. The constant α was then determined by adjusting the π^0-mass. The found value is $\alpha = 0.0142$ which agrees well with the value determined for the correction for the exclusive channels mentioned above. In the following table the values for the π^0- and η-masses as well as the mass difference $\Upsilon(2S)$-$\Upsilon(1S)$ are given before and after energy correction. The π^0-mass has the desired value while the η comes out somewhat too low and the mass difference $\Upsilon(2S)$-$\Upsilon(1S)$ a bit too high.

Mass (MeV) /PART84/	Energy (MeV) before correction	Energy (MeV) after correction
π^0 (134.96)	132.53 ± 0.14	134.96 ± 0.15
η (548.8)	531.2 ± 2.2	545.9 ± 2.4
$M(\Upsilon')-M(\Upsilon)$ (563.3)	551.5 ± 5.5	565.8 ± 5.5

Table 5. Masses before and after energy correction

Using these corrections for the energies as determined by the global fit one obtains the following results :

Energy (MeV)
110.6 ± 0.8
130.9 ± 0.8
163.3 ± 1.5

Table 6. Results for the global fit after energy correction

The error is statistical only. The systematic uncertainties are discussed in "Systematic Error on the Energies."

9.2 BRANCHING RATIOS

In order to calculate branching ratios from the observed signal amplitudes N_γ, one has to know the number of produced $\Upsilon(2S)$ resonance decays N_{res} as given in table 1 and the photon detection efficiency ε_γ. The branching ratio B is then calculated by using the following formula :

$$B = \frac{N_\gamma}{N_{res}\ \varepsilon_\gamma} \tag{18}$$

9.2.1 Photon Detection Efficiency

The Crystal Ball detector has a photon detection effiency for a single photon in the ball of nearly 100 %. The overlap with other particles,conversion in the beam pipe and the tube chambers or misidentification as a charged particle considerably reduce the possibility to detect a photon.

The photon selection program itself is the major factor in reducing the detection efficiency. After all cuts described above only 15 - 20 % of the photons remain (for photons evenly distributed over the full solid angle) slightly dependent on the energy of the γ.

The total photon detection efficiency is given by

$$\varepsilon_\gamma = \varepsilon_{mc}\ \varepsilon_{fs}\ (\ 1-\varepsilon_{conv}\ )\ \varepsilon_{ang} \tag{19}$$

where ε_{mc} takes into account all photon selection criteria.

The efficiency ε_{fs} gives the probability to observe a final state configuration consisting of hadrons and the monochromatic photon line. This number is found to be 90 ± 7 % using the same Monte Carlo models as used for the determination of the hadron selection efficiency (see "Hadron Selection Efficiency").

ε_{conv} is the conversion probability of photons into an electron positron pair in the material which is in front of the outer layer of the tube chambers. This number was calculated from the thickness (in radiation lengths) of the beam pipe and the first 2

layers of tubes as explained in "Tube chambers" and is 4.6 ± 0.4 %.

ε_{ang} reflects the change in the detection efficiency due to the angular distribution of the photons depending on the spins of the ^3P_J states.

If one assigns angular momenta to the 3 low energy lines and uses the calculated angular distributions /BROW76/ for the different lines instead of flat ones,one has to correct the amplitudes by the factors in table 7 (within the limited solid angle of $|\cos\Theta| < .75$ used in this analysis)

Transition	Angular Distribution	Correction Factor
$\Upsilon(2S) \to \gamma\, ^3P_0$	$W(\Theta) \propto 1 - \cos^2\Theta$	0.891
$\Upsilon(2S) \to \gamma\, ^3P_1$	$W(\Theta) \propto 1 - 1/3\ \cos^2\Theta$	1.054
$\Upsilon(2S) \to \gamma\, ^3P_2$	$W(\Theta) \propto 1 + 1/13\ \cos^2\Theta$	0.989

Table 7 : Correction factors for angular distributions

9.2.1.1 Determination of the Photon Selection Efficiency

The method to calculate the photon selection efficiency ε_{mc} is not totally based on Monte Carlo calculations but on a mixture of Monte Carlo and real events.

Monochromatic photons were generated by the EGS Monte Carlo code /FORD78/ in the energy range of 90 - 500 MeV and propagated through the Crystal Ball geometry not simulating the tube chambers. The energy of one of these photons is then added to a real $\Upsilon(1S)$ event. This merged event is analyzed by the production software and later on by the photon selection program. One uses the assumption that the decays of 1^3P_J states and $\Upsilon(1S)$ should be sufficiently similar and that the recoil of the photon only has a small effect on the recoiling system that one does not have to worry about the correct simulation of such events. As the $\Upsilon(2S)$ data taking was interspersed with $\Upsilon(1S)$ running one can expect that machine,detector and chamber performances are simulated more realistically by this method than by creating Monte Carlo events

Fits were performed to the photon line added to the γ-spectrum to determine ε_{mc} by dividing the number of found Monte Carlo photons by the number of originally merged γ into the data sample.

The resulting ε_{mc} are shown in Figure 30 for the succesive cuts. The systematic error was determined by merging lines into $\Upsilon(2S)$, $\Upsilon(1S)$ and continuum events.

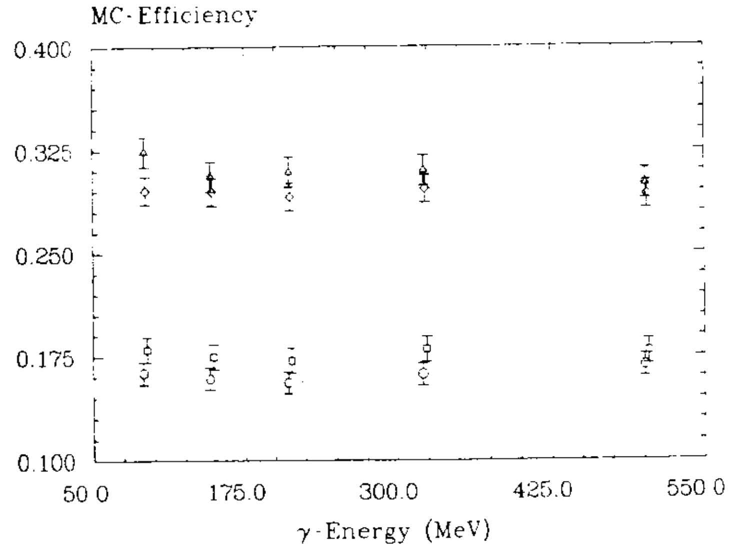

Figure 30 The photon selection efficiency for succesive cuts, corresponding to cuts 2,3,4,5 as mentioned in the text from top to bottom (only statistical errors are given)

Combining all efficiencies ε_γ is determined to be :

Energy Range	Efficiency
110 MeV	13.6 ± 2.4
131 MeV	14.5 ± 2.6
163 MeV	12.2 ± 3.1
430 MeV	13.7 ± 2.1

Table 8 : Efficiencies

9.2.2 Results

The branching ratios for the 3 low energy lines are listed in table 9 together with the product branching ratio for the sum of two Doppler broadened lines (mean energy at 430 MeV).

Energy (MeV)	Branching ratio (%)
110	5.9 ± 0.7
131	6.5 ± 0.6
163	3.7 ± 0.7
430	3.4 ± 0.7

Table 9. Branching ratios determined from the global fit with the statistical errors only

10.0 SYSTEMATIC ERRORS

So far only the statistical error was given for the energies and branching ratios of the observed lines. The systematic errors which mainly come from the fitting procedure will be discussed in the following sections.

10.1 SYSTEMATIC ERROR ON THE ENERGIES

In order to determine the systematic error on the energy, the same fit as done for the final spectrum was performed after each successive step of the photon selection. The results can be seen in Figure 31. The variation of the energies was used to estimate the effect of the cuts on the energy and the size of the systematic error. One can conclude that the energies of the lines do not depend on the used cuts to extract them because there are no large fluctuations.

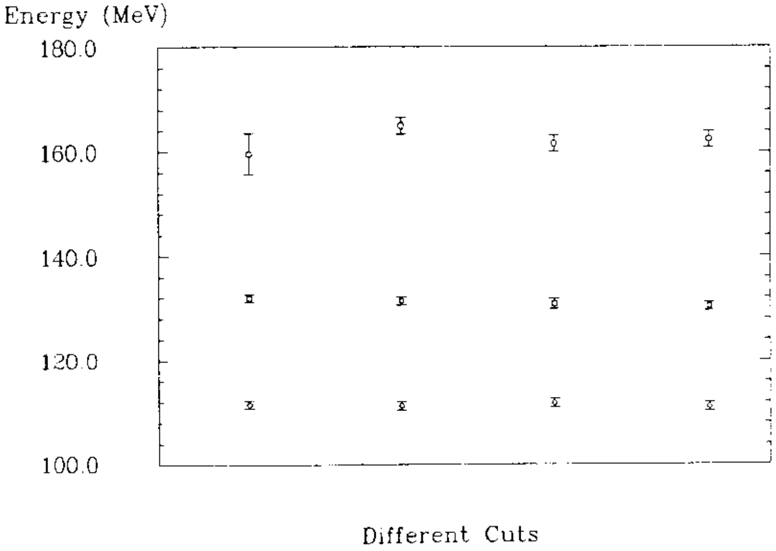

Figure 31. Energy dependence of the lines for the different cuts corresponding to cuts 2,3,4 and 5 of the photon selection from left to right

Another important parameter for the fit is the number of charged particles in the final spectrum. The dependence of the systematic error for the energies on this variable is found by varying the content of punchthrough in the global fit to the inclusive photon spectrum. Compared are the ratios of energies which were determined by the global fit and the energies found with a fixed amount of punchthrough and can be seen in Figure 32. For the energies the introduced errors by using a wrong number for the punchthrough are negligible.

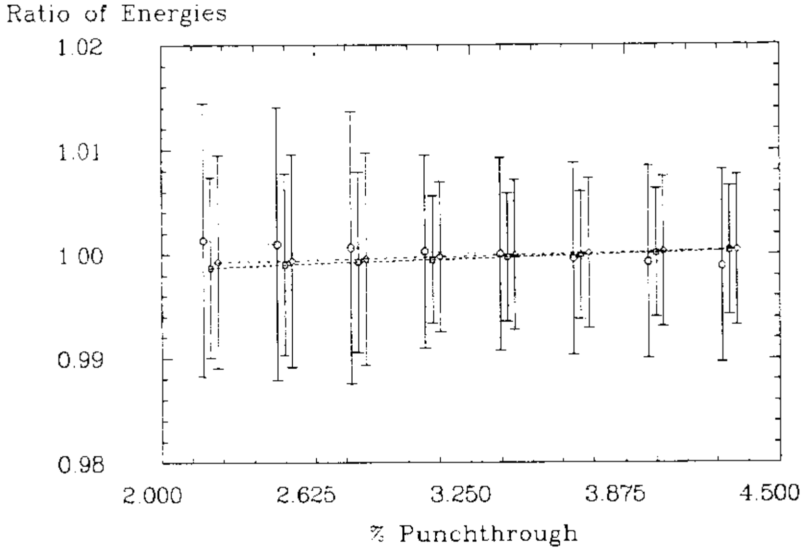

Figure 32. Energy dependence for different amounts of charged particles (○ = 163 MeV, □ = 131 MeV, ◇ = 110 MeV lines)

The uncertainty in the absolute energy scale is estimated to be 1 MeV for the 3 low energy lines.

A systematic error due to a variation in the fitting procedure (e.g. a different fit window, different binning) amounts to 1 % of the measured energies.

Combining all systematic errors the overall systematic error for the energies is calculated to be 2.2, 2.4 and 2.7 MeV for the lines at 110, 131 and 163 MeV respectively.

10.2 SYSTEMATIC ERROR ON THE BRANCHING RATIOS

The systematic error on the branching ratios is calculated with the same methods used for the energies. The branching ratios should be independent of the energy corrections. On the other hand the charged particle background has a bigger influence on the branching fractions than on the energies, especially for the line around 163 MeV which is very dependent on the exact amount of punchthrough as shown below.

The first check was to perform the branching ratio calculations for the different stages of the photon selection. The results are shown in Figure 33.

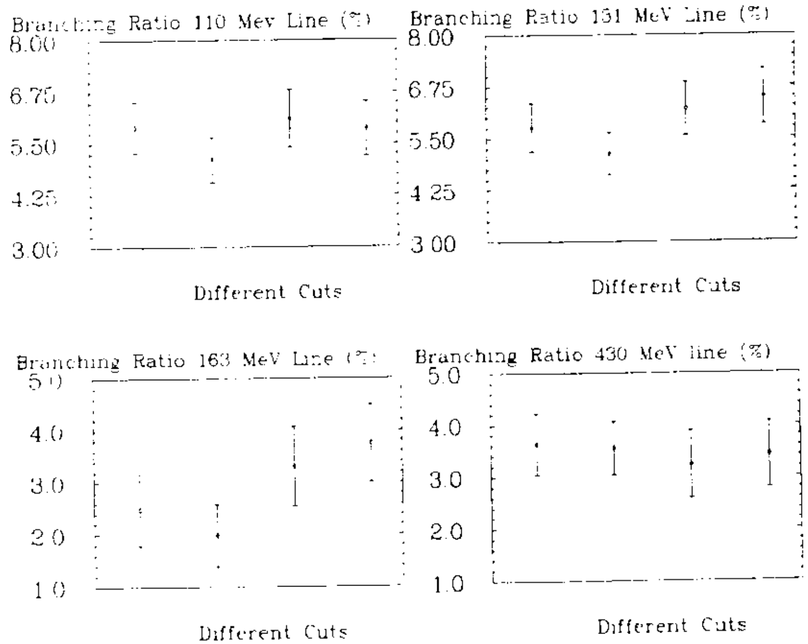

Figure 33 Branching ratios for the different stages of selection corresponding to cuts 2,3,4 and 5 of the photon selection from left to right.

One can see that the results for the different cuts agree within the errors.

The other check was to vary the punchthrough and determine the resulting branching ratios as can be seen in Figure 34 where the branching ratio found for a fixed amount of punchthrough is divided by the number found by the global fit.

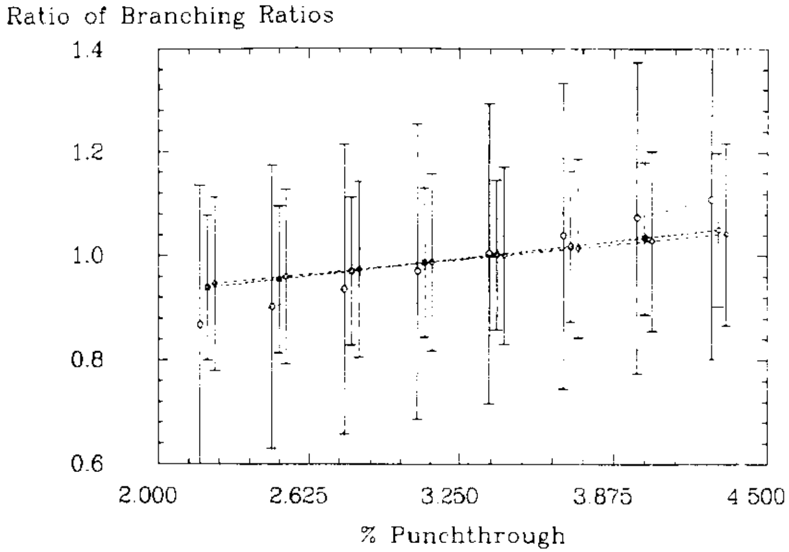

Figure 34. Variation of the branching ratios with respect to punchthrough (O = 163 MeV, □ = 131 MeV, ◇ = 110 MeV lines)

One can see that the line around 163 Mev has by far the largest fluctuation as expected by the closeness to the punchthrough region.

Combining these errors with the systematic errors for the photon detection efficiency, the number of resonance decays and errors introduced by the fitting procedure, the systematic errors for the branching ratios are found to be 1.0 %, 1.2 % and 0.9 % for the lines at 110, 131 and 163 MeV respectively.

11.0 CHECKS

11.1 Υ(1S) SPECTRUM

The same program used to extract the lines in the Υ(2S) spectrum was also used on Υ(1S) data (see Figure 35)

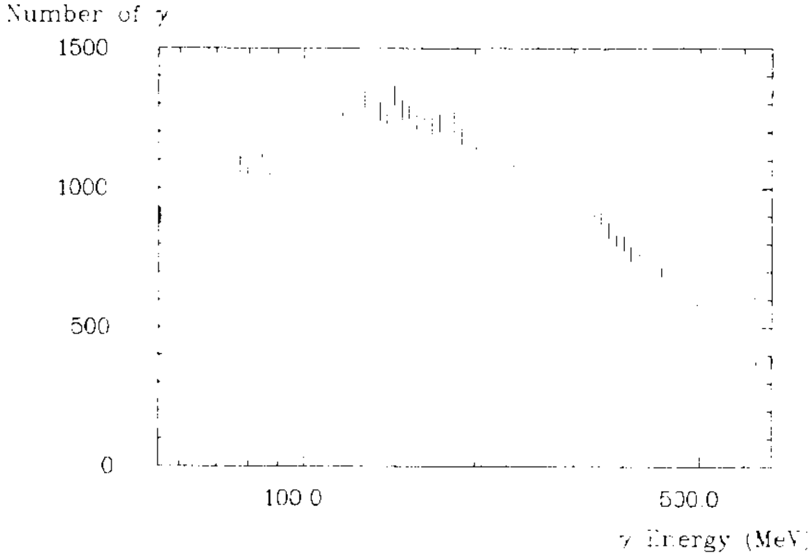

Figure 35. Inclusive photon spectrum from the Υ(1S)

No structure can be seen in the region of interest between 100 and 16[illegible] MeV and around 430 MeV. This shows that the lines in the Υ(2S) spectrum are not created by some software effect in the data analysis rather than being physics.

A similar spectrum for the continuum suffers from low statistics and is not shown here.

11.2 BACKGROUND FROM THE TRANSITION $\Upsilon(2S)$--> $\pi^0\pi^0\Upsilon(1S)$

Photons from the decay of π^0's resulting from the transition $\Upsilon(2S)$--> $\pi^0\pi^0\Upsilon(1S)$ should have some influence on the inclusive photon spectrum because roughly 9 % /BROC84/,/FONS84/ of the decays of the $\Upsilon(2S)$ resonance should proceed through this channel to the $\Upsilon(1S)$. If a photon from the π^0 decay into 2 γs cannot be reconstructed,survives the photon selection and shows up in the inclusive γ-spectrum of the $\Upsilon(2S)$ this might create a monochromatic line or other significant structures which might be mistaken to be the photon lines or the charged particle punchthrough.

In order to determine the exact amount and energy distribution of γ's in the final inclusive $\Upsilon(2S)$ spectrum,two Monte Carlo π^0's were generated and merged into $\Upsilon(1S)$ decays to simulate the total hadronic transition to the $\Upsilon(1S)$.

The $\pi\pi$ transition was modelled according to an invariant mass distribution as suggested by /YANO80/ and verified by various experiments for the neutral and charged transition /NICZ81/,/BROC84/,/MAGE81/,/FONS84/,/MUEL81/,/BESS84/ and /ALBR84/. The π^0's each decay into 2 photons which are simulated to shower in the detector.

A rather characteristic peaking of the energy spectrum of photons surviving all cuts around 200 MeV can be seen in Figure 36 but there are no monochromatic lines. If one subtracts the correct amount of remnants due to this transition from the inclusive photon spectrum as done in Figure 37, one can see that this effect is negligible and that there is no apparent structure which is added or caused by this transition.

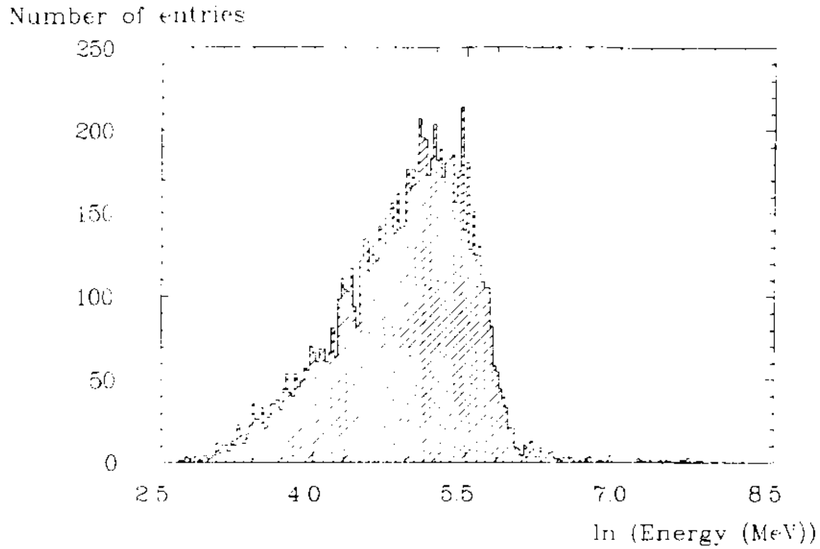

Figure 36. Photon spectrum due to the hadronic cascade via $\pi^0\pi^0$ in the final inclusive γ-spectrum

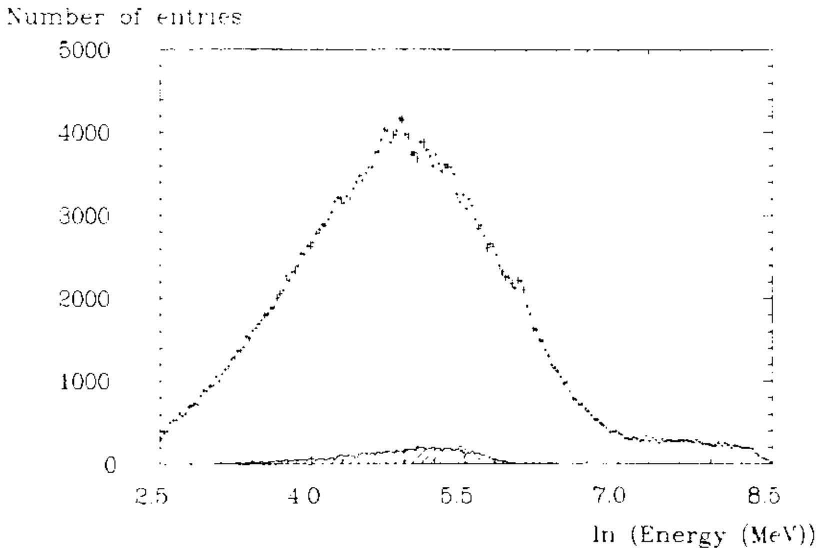

Figure 37. Photon spectrum with subtraction of $\pi^0\pi^0$-transition (shaded=subtracted spectrum)

To check if the amount of charged particles in the final γ spectrum of the $\Upsilon(2S)$ found by the global fit was determined correctly another method was applied. This was done by using a strong pattern cut which is especially suited to identify patterns of minimum ionizing particles. It cuts very hard on low energies which makes it unsuitable for the inclusive analysis of the lines around 100–165 MeV. Therefore this cut is only used to determine the punchthrough in the final spectrum around 210 MeV. If one plots the transmission efficiency (number of particles per energy bin surviving the cut divided by the number before the cut) for charged particles as a function of the shower energy,one can see a strong dip at energies corresponding to minimum ionizing particles (Figure 38).

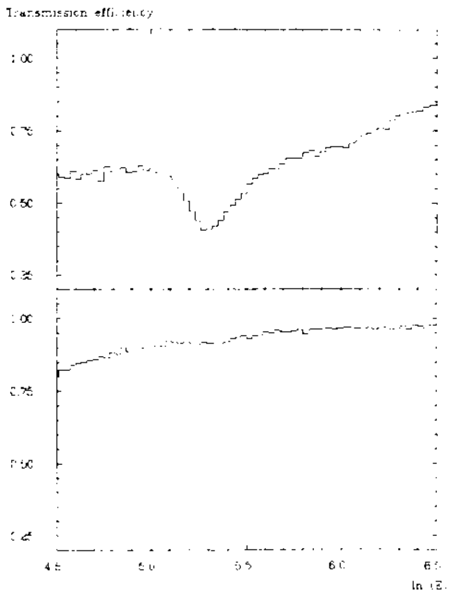

Figure 38. The transmission efficiency for charged and neutral particles (bottom) selected by the same cuts of the photon selection

The same plot for photons should show a smooth curve. In the real spectrum with charged track contamination,one can still see a small dip around 210 MeV. The magnitude of it is proportional to the amount of charged track contamination and can be measured in the following way.

One uses a series of plots where the transmission efficiency for photons is plotted for varying amounts of charged particles subtracted in order to determine at which value one reaches a smooth transmission curve which should correspond to the exact amount of punchthrough in the final γ-spectrum.

In order to determine the amplitude of the peak these curves are fitted by a single gaussian over a smooth polynomial background as one can see from Figure 39.

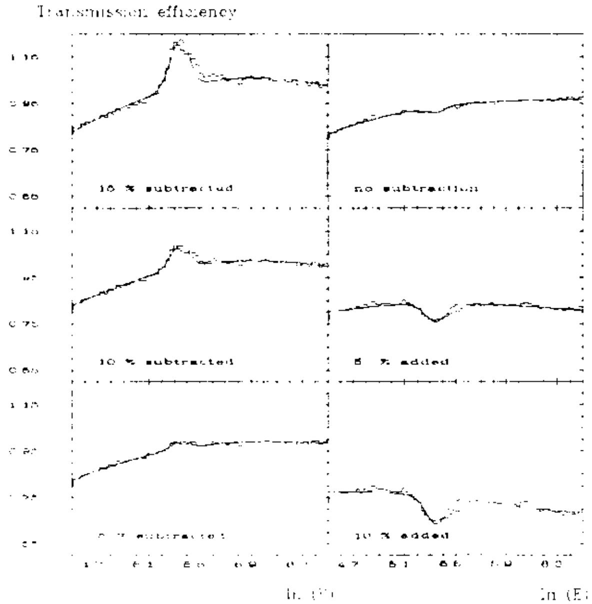

Figure 39. The transmission efficiency for different amounts of background subtracted

The results of the fits can bee seen in Figure 40 where the found amplitudes are plotted as a function of the charged particle content. The final number for the punchthrough is obtained by fitting the different points by a straight line and determining the point where the amplitude is zero.

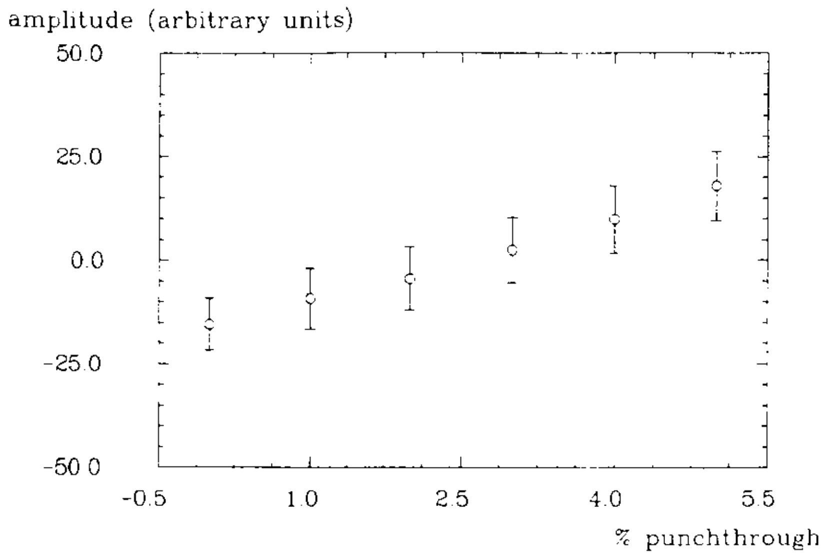

Figure 40. Resulting amplitudes of charged particles

The resulting number for the punchthrough determined by this method is 2.64 ± 0.75 % which is slightly lower but still compatible with the number found in the global fit to the $\Upsilon(2S)$ inclusive photon spectrum of 3.35 ± 0.85 %. The difference between these 2 numbers gives an estimate of the systematic error for the punchthrough.

12.0 FINAL RESULTS

The final numbers for the energies and branching ratios obtained from the inclusive photon spectrum of the hadronic decays from the $\Upsilon(2S)$ are obtained to be

Energy
110.6 ± 0.8 ± 2.2 MeV
130.9 ± 0.8 ± 2.4 MeV
163.3 ± 1.5 ± 2.7 MeV

Table 10. : Results for the energies obtained in the global fit after energy correction with statistical (first) and systematic (second) error

Energy (MeV)	Branching ratio (%)
110	5.9 ± 0.7 ± 1.0
131	6.5 ± 0.6 ± 1.2
163	3.7 ± 0.7 ± 0.9
430	3.4 ± 0.7 ± 0.5

Table 11. : Branching ratios determined from the global fit with the statistical (first) and systematic (second) error

No other photon lines were observed with statistical significances of more than 1.3 standard deviations in the energy range 50 - 100 MeV giving upper limits for branching ratios of 2.6 % (90 % c.l.) nor in the range 450 - 8[illegible]0 giving upper limits of 0.7 % (90 % c.l.) assuming flat angular distributions.

12.1 COMPARISION WITH OTHER EXPERIMENTS

In table 12 a comparision of the energies of photon lines obtained by the Crystal Ball and the experiments ARGUS (preliminary) /SCHR84/, CLEO /HAAS84/, CUSB /KLOP83/ is given as well as a weighted mean of the energies.

Experiment	$^3P_2$	$^3P_1$	$^3P_0$
CB	110.6 ± 0.8 ± 2.2	130.9 ± 0.8 ± 2.4	163.3 ± 1.5 ± 2.7
CUSB	108.2 ± 0.3 ± 2.0	128.1 ± 0.4 ± 3.0	149.4 ± 0.7 ± 5.0
CLEO	109.5 ± 0.7 ± 1.0	129.0 ± 0.8 ± 1.0	*158.0 ± 7.0 ± 1.
ARGUS	109.0 ± 1.0 ± 1.0	129.8 ± 0.8 ± 1.0	*147.2 ± 1.4 ± 1.
Mean value	109.4 ± 0.8	129.6 ± 0.8	159.4 ± 2.6

Table 12. : Energies found by 4 different experiments and an averaged mean of all 4 measurements.(* means that the value is not used for the average value)

In table 13 the branching ratios for the 3 low energy lines as measured by 4 experiments in their inclusive photon spectra are listed together with their weighted means.

Experiment	$^3P_2$	$^3P_1$	$^3P_0$
CB	5.9 ± 0.7 ± 1.0	6.5 ± 0.6 ± 1.2	3.7 ± 0.7 ± 0.9
CUSB	6.1 ± 1.4	5.9 ± 1.4	3.5 ± 1.4
CLEO	10.2 ± 1.8 ± 2.1	8.0 ± 1.7 ± 1.6	*4.4 ± 2.3 ± 0.9
ARGUS	8.9 ± 3.0 ± 1.2	8.8 ± 2.2 ± 1.0	*4.0 ± 1.8 ± 1.0
Mean value	6.7 ± 0.8	6.8 ± 0.8	3.6 ± 0.9

Table 13. : Branching ratios found by 4 different experiments with statistical (first) and systematic (second) errors (* means that the value is not used for the average value).

A graphical representation of the results can be seen in Figure 41,where the experimental energies are plotted with their corresponding branching ratios. The statistical and systematic errors are added in quadrature to give the plotted errors.

One can see that within the experimental errors there is agreement among the several analyses for the lines around 109 and 129 MeV but differences in the energy of the line around 147-163 MeV. This might be due to the low significances of the lines found by some of the experiments. The CLEO-collaboration reports a significance of less than 2 standard deviations stating that a third line is not clearly implied by their data. The ARGUS-group gives a significance of 2.2 standard deviations with very small errors. This value would dominate the averaging process for a line around 149-163 MeV. Therefore these two measurements are excluded from the calculation of the mean energies and branching ratios.

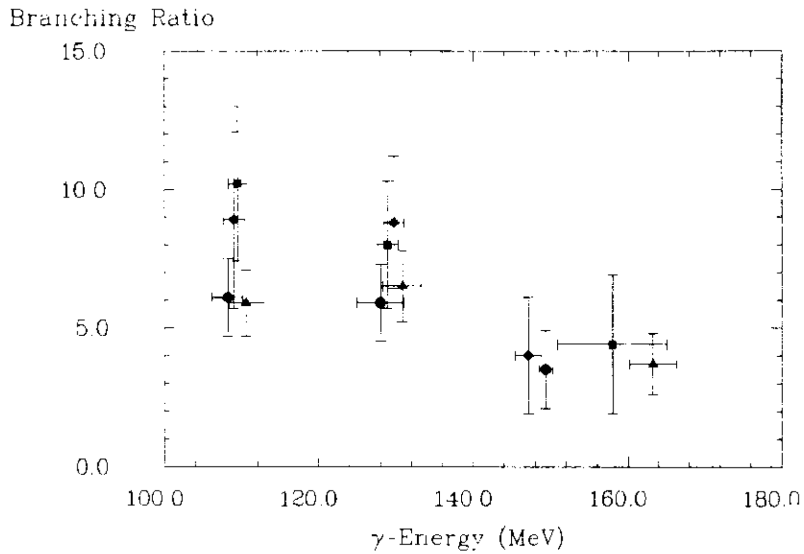

Figure 41. Energies and branching ratios for 4 different experiments ▲ = (Crystal Ball),■ = (CLEO),◆ = (ARGUS),● = (CUSB)

For the secondary lines from the ^3P_J states to the $\Upsilon(1S)$ only the CUSB- and Crystal Ball-collaborations give results which are summarized in table 14 :

Experiment	Branching ratio (%)
Crystal Ball	3.4 ± 0.7 ± 0.5
CUSB	4.0 ± 1.0
Mean value	3.7 ± 0.7

Table 14. : Branching ratios for the secondary lines

These results can be compared with the product branching ratios from the exclusive analyses

$\Upsilon(2S) \to \gamma\gamma l^+l^-$, leptons from $\Upsilon(1S)$

by CUSB /PAUS83/ and Crystal Ball/BROC84/ where one has to know the leptonic branching ratio of the $\Upsilon(1S)$ in order to calculate the cascade branching fractions. The CUSB-value has been rescaled to take a value for the leptonic branching ratio of 2.9 % /PART84/ (instead of 2.8 %) which is the value given for the μ-pair branching ratio. This value is also used for the branching fraction into e^+e^- assuming lepton universality because of the much smaller errors. The results in the following table should be compared with the inclusive results and one can see good agreement among the measured values.

Experiment	Branching ratio (%)
Crystal Ball	4.2 ± 1.1
CUSB	3.5 ± 0.9

Table 15. : Branching ratios for the secondary lines for exclusive cascade transitions.

12.2 COMPARISION WITH THEORETICAL PREDICTIONS

The most important questions in comparing experiment and theory are :

What are the masses,the E1-transition rates and spins of the ^3P_J states. As pointed out in "$^3P_{2,1,0}$ States" the spins cannot be determined from the inclusive photon analysis but the transition rates and masses can be found.

Once these quantities are known one can find out which predictions and models fit the data best. Many models make predictions for the centre of gravity M_{cog} of the ^3P_J states which is defined in Eq.(11) . The centre of gravity is not very sensitive to the exact knowledge of the energy of the $^3P_0$ state because of the low weight. As one can see from the following table most of the newer predictions agree well with the measured value for the centre of gravity if one assumes an uncertainty in the absolute energy scale of about 10 MeV. The predictions by /EICH81/ and /MCCL83/ give rather high values.

Author	M(c.o.g.) (MeV)
Crystal Ball	9899.4 ± 2.0
/BUCH82/	9888.7
/BAND84/	9891.0
/MOXH83/	9906.2
/GUPT82/	9897.7
/KAHR81/	9871.0
/EICH81/	9924.7
/MCCL83/	9922.8

Table 16. : Theoretical predictions for the centre of gravity of the ^3P_J states The c.o.g. for /BUCH82/ has been rescaled by 27 MeV to use the correct $\Upsilon(1S)$ mass, /GUPT82/ by 2 MeV.

Predictions for the fine structure splitting of the ^3P_J states are fewer than for the centre of gravity. A variable parameterizing the fine structure splitting is

$$r = \frac{M(1^3P_2) - M(1^3P_1)}{M(1^3P_1) - M(1^3P_0)} \qquad (20)$$

where M are the masses of the different spin states. The advantage in using r is that most of the systematic errors cancel.

The systematic error on the mass difference of two lines as measured in the inclusive photon spectrum can be estimated by using the same methods as for the energies of the lines but this time the mass difference is plotted. The systematic error is calculated to be 1.4 for the difference of the masses $^3P_2$-$^3P_1$ and 1.8 MeV for the mass difference $^3P_1$-$^3P_0$ where the main contribution comes from the different fitting methods. The systematic error coming from the energy corrections is quite small.

In the following table the values for the mass differences $M(P_2)$-$M(P_1)$,$M(P_1)$-$M(P_0)$ and r from Crystal Ball results and theoretical predictions are compared.

Author	$M(P_2)$-$M(P_1)$	$M(P_1)$-$M(P_0)$	r
Crystal Ball	20.3 ± 1.8	32.4 ± 2.5	0.63 ± 0.10
BUCH82	31	41	0.76
BAND84	27	35	0.77
MOXH83	11	26	0.42
GUPT82	17	25	0.68
KAHR81	12	24	0.50
EICH81	26	25	1.04
MCCL83	22	49	0.45

Table 17 : Theoretical predictions for the masses of the ^3P_J states

One can see that it is not possible to distinguish between the different models by comparing the values for r which are in the range of 0.4 - 0.8 but the results disagree with higher predictions like /EICH81/.

It can also be seen that the value is far from r=2 (see "Potential Models") which indicates that one has to use tensor forces in order to describe the fine structure splitting of the 1^3P_J states.

Even fewer predictions can be found for the E1-transition rates to reach the 1^3P_J states from the Υ(2S). In table 18 the branching ratios predicted by theory and measured by the Crystal Ball are compared. The errors given for the theoretical predictions are only due to the uncertainty in the total width of the Υ(2S) which is taken to be 29.6 ± 4.7 keV /PART84/.

Author	B ($^3P_2$)	B ($^3P_1$)	B ($^3P_0$)
Crystal Ball	5.9 ± 1.2	6.5 ± 1.3	3.7 ± 1.1
/BUCH82	7.4 ± 1.2	9.1 ± 1.4	6.5 ± 1.1
/KAHR81	5.4 ± 0.9	3.6 ± 0.6	1.9 ± 0.3
/MOXH83/*	7.8 ± 1.2	7.4 ± 1.2	4.1 ± 0.7
/MCCL83/*	7.4 ± 1.2	6.7 ± 1.1	3.1 ± 0.5

Table 18. Predicted branching ratios (in %) in comparision with the Crystal Ball result. * means that the used energies for the predictions are the experimental ones from 4 experiments as given in table 12

The experimentally found values are in agreement with most of the theoretical predictions so that one cannot distinguish between the different approaches for the potentials by means of the branching ratios,either.

13.0 CONCLUSIONS

Four well resolved lines are observed in the inclusive photon spectrum from hadronic decays of the $\Upsilon(2S)$. A coherent picture is obtained when these lines are interpreted as resulting from E1-transitions $\Upsilon(2S) \rightarrow \gamma\ {}^3P_{2,1,0}$ and ${}^3P_{2,1} \rightarrow \gamma\Upsilon(1S)$. By clearly resolving all three low energy lines and observing the photon line around 163 MeV with a large statistical significance a complete measurement of the fine splitting of the $1^3P_{2,1,0}$ states of the Υ $b\bar{b}$ system has been made.

No evidence for lines other than the above mentioned was found.

14.0 REFERENCES

/ALBR84/ H.Albrecht et al.,Phys.Lett. 134B,137 (1980)

/ANDR80/ D.Andrews et al.,Phys.Rev.Lett. 44,1108 (1980)

/ANDR80a/ D.Andrews et al.,Phys.Rev.Lett. 45,219 (1980)

/ARTA82/ A.S.Artamonov et al.,Phys.Lett. 118B,225 (1982)

/ARTA84/ A.S.Artamonov et al.,Phys.Lett. 137B,272 (1984)

/BAND84/ M.Bander et al.,Phys.Lett. 134B,258 (1984)

/BARB84/ D.P.Barber et al.,Phys.Lett. 135B,498 (1984)

/BEBE81/ C.Bebek et al.,Phys.Rev.Lett. 46,84 (1981)

/BERG78/ C.Berger et al.,Phys.Lett. 76B,243 (1978)

/BESS84/ D.Besson et al.,Phys.Rev.D30,1433 (1984)

/BIEN78/ J.K.Bienlein et al.,Phys.Lett. 78B,360 (1978)

/BHAN78/ G.Bhanot et al.,Phys.Lett. 78B,119 (1984)

/BÖHR80/ T.Böhringer et al.,Phys.Rev.Lett. 44,1111 (1980)

/BROC84/ I.Brock,Dep.Part.&Fields,APS-meeting Santa Fe,NM 1984

/BROW76/ L.S.Brown,R.N.Cahn et al.,Phys.Rev.D13,1195 (1976)

/BUCH80/ W.Buchmüller et al.,Phys.Lett.45B,103 (1982),587(E)('80)

/BUCH81/ W.Buchmüller,S.H.H.Tye,Phys.Rev.D24,132 (1981)

/BUCH82/ W.Buchmüller,Phys.Lett. 112B,479 (1982)

/CHAD81/ K.Chadwick et al.,Phys.Rev.Lett. 46,88 (1981)

/CHAN78/ Y.Chan et al.,IEEE Trans. Nucl.Sci.25,333(1978)

/CHES79/ R.Chestnut et al.,IEEE Trans. Nucl.Sci.26,4395(1979)

/DARD78/ C.W.Darden et al.,Phys.Lett 76B,246 (1978)

/DARD78a/ C.W.Darden et al.,Phys.Lett. 78B,364 (1978)

/DORI79/ DORIS Storage Ring Group,DESY Report 70/08 (1979)

/EICH80/ E.Eichten et al.,Phys.Rev.D21,203 (1980)

/EICH81/ E.Eichten,F.Feinberg,Phys.Rev.D23,2724 (1981)

/EIGE82/ G.Eigen et al.,Phys.Rev.Lett 49,1616 (1982)

/FINO80/ G.Finocchiaro et al.,Phys.Rev.Lett. 45,222 (1980)

/FONE84/ V.Fonesca et al.,Nucl.Phys. B242,31 (1984)

/FORD78/ R.L.Ford,W.R.Nelson,SLAC Report No.210 (1978)

/FRID84/ A.Fridman ,Inv.talk at 6th Int. Symp. on High Energy Spin Physics Marseille,France 1984

/GABR81/ T.A.Gabriel et al.,Oak Ridge Nat.Lab.Report ORNC/TM 7123-81

/GAIS82/ J.E.Gaiser,Ph.D. thesis,SLAC Report No.255 (1982)

/GALI83/ R.S.Galik,in the Proceedings of the Int.Europhysics Conf. on High Energy Physics,Brighton (1983)

/GELL64/ M.Gell-Mann,Phys.Lett 8,214 (1964)

/GREE82/ J.Green et al.,Phys.Rev.Lett. 49,617 (1982)

/GUPT82/ S.N.Gupta et al.,Phys.Rev D26,3305 (1982)

/HAAS84/ P.Haas et al.,Phys.Rev.Lett. 52,799 (1984)

/HANO82/ K.Han et al.,Phys.Rev.Lett. 49,1612 (1982)

/HERB77/ S.W.Herb et al.,Phys.Rev.Lett. 39,252 (1977)

/HORI84/ R.P.Horisberger,Ph.D. thesis,SLAC Report No.266 (1984)

/INNE77/ W.R.Innes et al.,Phys.Rev.Lett. 39,1240 (1977)

/IRIO84/ J.Irion,in the Proceedings of the Recontre de Moriond, La Plagne (1984)

/JACK75/ J.D.Jackson,D.L.Scharre,Nucl.Inst.&Meth. 128,13 (1975)

/KAHR81/ A.Kahre,Phys.Lett.98B,385 (1981)

/KIRK79/ G.I.Kirkbride et al.,IEEE Trans. Nucl.Sci.26,1535(1979)

/KLOP83/ C.Klopfenstein et al.,Phys.Rev.Lett. 51,160 (1983)

/KRAS79/ H.Krasemann,Z.Phys.C1,189 (1979)

/MACK84/ W.W.MacKay et al.,Phys.Rev.D29,2483 (1984)

/MAGE81/ G.Mageras et al.,Phys.Rev.Lett. 46,1115 (1981)

/MART80/ A.Martin,Phys.Lett 93B,338 (1980)

/MASC84/ W.Maschman,Diplomarbeit Universität Hamburg (1984)

/MCCL83/ R.McClary,N.Byers,Phys.Rev.D28,1692 (1983)

/MOXH83/ P.Moxhay,J.L.Rosner,Phys.Rev.D28,1132 (1983)

/MUEL81/ J.J.Mueller et al.,Phys.Rev.Lett. 46,1181 (1981)

/NESE83/ H.Nesemann,K.Wille,DESY M-83-26 (1983)

/NICZ81/ B.Niczyporuk et al.,Phys.Lett. 100B,95 (1981)

/NOVI78/ V.A.Novikov,Phys.Rep 41C,1 (1978)

/OKUB63/ S.Okubo,Phys.Lett. 5,165 (1963)
G.Zweig,CERN TH 401,412 (1964)
J.Iizuka,Progr.Theor.Phys.Suppl. 37-[illegible] 21 (1966)

/OREG80/ M.J.Oreglia,Ph.D. thesis,SLAC Report No.2[illegible] (1980)

/PART84/ Particle Data Group,Mod.Phys. 56,No.2 Part [illegible] (1984)

/PART84/ Particle Data Group,Mod.Phys. 56,No.2,Part II (1984)

/PAUS83/ F.Pauss et al.,Phys.Lett. 130B,439 (1983)

/QUIG77/ C.Quigg,J.L.Rosner,Phys.Lett.71B,153 (1981)

/RPAR80/ R.Partridge et al.,Phys.Rev.Lett. 45,1150 (1980)

/RPAR84/ R.Partridge,Ph.D. thesis,CALT-68-1150 (1984)

/RICH79/ J.L.Richardson,Phys.Lett 82B,272 (1979)

/SCHW83/ A.Schwarz,in the Proceedings of the Int.Europhysics Conf. on High Energy Physics,Brighton (1983)

/SCHR84/ H.Schröder,Results presented at the XXII Int. Conf. on High Energy Physics,Leipzig (1984)

/SIEV85/ D.Sievers,Diplomarbeit Universität Hamburg (1985)

/SJÖS84/ T.Sjöstrand,DESY Report T-84-01 and 84-19 (1984)

/TUTS83/ M.Tuts,Results presented at Int. Symp. on Lepton and Photon Interactions at High Energies,Cornell (1983)

/YANO80/ T.M.Yan,Phys.Rev.D22,1652 (1980)

ACKNOWLEDGEMENTS

I would like to thank the entire Crystal Ball collaboration* without whose efforts this work could not have been accomplished.

Special thanks go to my advisor Prof.Dr.U.Strohbusch for his encouragement and fruitful discussions, to Dr.J.Irion and Dr.A.Schwarz for their cooperation and many suggestions, to the members of the CB group belonging to the I.Institut für Experimentalphysik der Universität Hamburg for providing a pleasant working atmosphere and to the people at SLAC for their friendly help during my time there.

Financial support was provided by the Bundesministerium für Forschung und Technologie.

* The members of the Crystal Ball collaboration were :

D.Antreasyan, D.Aschman, D.Besset, J.K.Bienlein, E.D.Bloom, I.Brock, R.Cabenda, A.Cartacci, M.Cavalli-Sforza, R.Clare, G.Conforto, S.Cooper, R.Cowan, D.Coyne, D.de Judicibus, C.Edwards, A.Engler, G.Folger, A.Fridman, J.Gaiser, D.Gelphman, G.Godfrey, F.H.Heimlich, R.Hofstadter, J.Irion, Z.Jakubowski, S.Keh, H.Kilian, I.Kirkbride, T.Kloiber, W.Koch, A.C.König, K.Königsmann, R.W.Kraemer, R.Lee, S.Leffler, R.Lekebusch, P.Lezoch, A.M.Litke, W.Lockman, S.Lowe, B.Lurz, D.Marlow, W.Maschmann, T.Matsui, F.Messing, W.C.Metzger, B.Monteleoni, R.Nernst, C.Newman-Holmes, B.Niczyporuk, G.Nowak, C.Peck, P.G.Pelfer, B.Pollock, F.C.Porter, D.Prindle, P.Ratoff, B.Renger, C.Rippich, M.Scheer, P.Schmitt M.Schmitz, J.Schotanus, A.Schwarz, D.Sievers, T.Skwarnicki, K.Strauch, U.Strohbusch, J.Tompkins, H.-J.Trost, R.T.Van de Walle, H.Vogel, U.Volland, K.Wacker, W.Walk, H.Wegener, D.Williams, P.Zschorsch